On an averaged model for immiscible two-phase flow with surface tension and dynamic contact angle in a thin strip

S.B. Lunowa, C. Bringedal, I.S. Pop

ON AN AVERAGED MODEL FOR IMMISCIBLE TWO-PHASE FLOW WITH SURFACE TENSION AND DYNAMIC CONTACT ANGLE IN A THIN STRIP

STEPHAN B. LUNOWA*, CARINA BRINGEDAL†, AND IULIU SORIN POP*

October 22, 2020

Abstract. We consider a model for the flow of two immiscible fluids in a two-dimensional thin strip of varying width. This represents an idealization of a pore in a porous medium. The interface separating the fluids forms a freely moving interface in contact with the wall and is driven by the fluid flow and surface tension. The contact line model incorporates Navier slip boundary conditions and a dynamic and possibly hysteretic contact angle law. We assume a scale separation between the typical width and the length of the thin strip. Based on asymptotic expansions, we derive effective models for the two-phase flow. These models form a system of differential algebraic equations for the interface position and the total flux. The result is Darcy-type equations for the flow, combined with a capillary pressure - saturation relationship involving dynamic effects. Finally, we provide some numerical examples to show the effect of a varying wall width, of the viscosity ratio, of the slip boundary condition as well as of having a dynamic contact angle law.

Key words. Asymptotic expansions; Two-phase flow; Freely moving interface; Dynamic contact angle; Thin strip; Upscaled models

AMS subject classifications. 35C20, 76M45, 35Q30, 76D05, 76D45

1. Introduction. Many industrial and environmental processes, such as oil recovery, geological CO_2 sequestration or groundwater pollution, strongly depend on the flow in the respective porous medium. In all these applications, it is necessary to describe the flow of all involved fluid phases at a macroscopic scale to allow for efficient simulations in large domains. In particular, the complex pore structure and the exact distribution of fluids are simplified into a representation by averaged quantities such as the porosity and saturation. The relations between these macroscopic quantities must be expressed with the help of effective parameters, which should combine all pore-scale effects. However, in many state-of-the-art models these parameters are postulated and not derived from a pore-scale model.

One of the earliest models for the macro-scale flow in a porous medium was proposed by Darcy [18]. Based on column experiments for fully-saturated, single-phase flow in a porous medium, a proportionality between the pressure gradient and the velocity was observed, involving the medium's permeability as proportionality factor. Subsequently, further experiments by Richards [59] and by Morrow and Harris [52] extended the theory to unsaturated and two-phase flow in porous media, respectively. The resulting flow models still include Darcy's law, with a then saturation-dependent permeability. However, they additionally involved the phase-pressure difference, also known as the capillary pressure, which appears due to surface tension between the phases.

Based on experiments at equilibrium conditions, nonlinear, but monotonic capillary pressure - saturation functions have been used for decades. However, already

---
*UHasselt – Hasselt University, Computational Mathematics, Agoralaan, 3590 Diepenbeek, Belgium (stephan.lunowa@uhasselt.be, orcid.org/0000-0002-5214-7245; sorin.pop@uhasselt.be, orcid.org/0000-0001-9647-4347)

†University of Stuttgart, Department of Hydromechanics and Modelling of Hydrosystems, Pfaffenwaldring 61, 70569 Stuttgart, Germany (carina.bringedal@iws.uni-stuttgart.de, orcid.org/0000-0003-0495-2634)

Morrow and Harris [52] showed that this relation also depends on the process — imbibition or drainage. Besides this hysteresis, further dynamic effects were reported in many experiments [24, 64, 20, 13, 74], leading to a variety of non-monotonic curves which cannot be combined into a simple capillary pressure - saturation function.

To overcome the mismatch between the experimental results and the mathematical models, several extensions of the capillary pressure - saturation relation have been proposed. Typically, dynamic effects and hysteresis are directly expressed in terms of spatial or temporal derivatives of the saturation leading to different capillary pressure models, e.g. [53, 6, 7, 8], for an overview see [61]. Alternatively, the interfacial area was introduced as an additional state variable leading to a capillary pressure - saturation - interfacial area relationship that implicitly models the dynamic and hysteretic effects via the change in interfacial area [29, 30]. Other hysteresis models are based on the concept of percolating/nonpercolating phases [31, 32, 33]. These extended models are able to reproduce non-monotonic phenomena like saturation overshoot and fingering as shown in [69, 70, 51] by qualitative analysis using a travelling wave approach and in [21, 46, 34, 41, 60, 75] by numerical simulations.

However, all models discussed above are considering the so-called Darcy scale, and thus describe the average behaviour of the liquid phases disregarding the detailed pore structure and processes at the pore scale. It is crucial to understand the dependence of the effective parameters on the underlying pore structure. At the pore scale, the mathematical model can incorporate the detailed physical processes, but it is posed in the entire pore space, which is extremely complex, and needs to account for all interfaces between phases. Resolving the whole complicated pore space of realistic scenarios in direct numerical simulations is infeasible, so that further simplifications are necessary to link the properties of the different scales.

To approach this task, there exist a large variety of analytical upscaling techniques, see [17] for an overview. The volume averaging method has been used to derive effective equations for quantities at the level of a representative elementary volume, while restricting the form of constitutive equations using the second law of thermodynamics at the Darcy scale. This method has been successfully applied to single-phase and two-phase flow in porous media in [28, 73, 55]. However, the technique does only provide explicit expressions for the effective parameters in the constitutive equations via closure problems, when additional assumptions are made. Alternatively, the homogenization method is a (matched) asymptotic expansion approach for typically periodic systems, where there is a clear scale separation. The idea is to approximate the problem involving a small parameter ε (e.g. the ratio of an average pore diameter to a Darcy-scale length) by the limit problem and its solution as $\varepsilon \to 0$. For an introduction to this method, we mention [36] and the references therein. Many results for flow in porous media have been obtained by homogenization, see e.g. [3, 1, 2, 48, 50, 49, 62], leading either to explicit expressions or to so-called cell problems for the effective parameters. In both cases, knowledge of the underlying pore structure allows for the explicit computation of the effective parameters. Therefore, we apply the homogenization method to explicitly derive effective relations.

Here we consider a simplified geometry, namely the flow through a single, long and thin pore as a representative for the porous medium. Despite the very simplistic representation, the upscaling of thin-strip models typically leads to Darcy-scale models with the same structure as well-recognized Darcy-scale models in general porous media, see e.g. [50, 49, 54, 62]. Additionally, using a single pore allows for the explicit derivation of closed-form expressions for the upscaled quantities. We assume that the pore is filled by two incompressible and immiscible fluid phases. The interface

separating the two fluids is traversal to the flow direction. The mathematical model consists of conservation laws for mass and momentum in time-dependent domains representing the fluids. Assuming a horizontal setting, we disregard gravity effects. The evolution of the interface separating the domains is not known a priori, but depends on the velocities of the fluids and on the surface tension between the fluids. Hence, the development of the boundary of the domains must be accounted for, and we have a free boundary problem.

While the fluid domains are assumed to be layered in [50, 49, 54, 62], such that the fluid-fluid interface does not come into contact with the solid wall, we here consider the case when the interface is in contact with the pore walls. This requires a contact angle model, which is allowed to be dynamic or even hysteretic. In particular, this also implies that each fluid is only present either at the inlet or at the outlet. Note that the plug flow scenario considered in [54] has a similar fluid distribution, but the authors assume a fixed interface shape and a residual thin-film, which yields dynamics that are very different from those generated by a variable interface with moving contact line. Furthermore, we allow for a slowly varying solid wall instead of a constant-width strip or tube used in [50, 49, 54, 62].

Based on the discussed pore-scale model, we derive upscaled (Darcy-scale) models for two-phase or unsaturated single-phase flow in a porous medium under reasonable assumptions on the underlying physics. We follow the ideas in [50, 49, 62], where asymmetric expansions and transversal averaging is applied to obtain a macro-scale model based on the simple, layered pore. We complement this with volume averages to account for the different geometry and fluid distribution. A similar strategy has been used to show that the upscaled models significantly differ for different flow regimes assuming stationary fluid-fluid interface shapes in [54], and in [62] when assuming a layered, parallel flow regime. In general, the thin-strip approach allows the derivation of explicit relations between the averaged quantities, while various additional features and processes can be easily incorporated, see e.g. [62, 71, 45, 14].

This paper is organized as follows. In section 2 we formulate the mathematical model for two-phase flow with evolving interface in a thin strip, which is then rescaled to obtain a non-dimensional formulation. Next, we formally derive in section 3 the effective models in the bulk domains and close to the interface when the ratio between the width and length of the thin strip approaches zero. These models form a system of differential algebraic equations for the interface position and the total flux. Based on the derived models, we discuss averaged and effective quantities and their relations in section 4. In particular, there holds a Darcy-type equation for the flow and a capillary pressure - saturation relationship involving dynamic effects. Finally, section 5 provides some numerical examples showing the behaviour of the effective models for a constant as well as a varying wall width. The effect of the viscosity ratio, of the slip length and of having a dynamic contact angle law are discussed in detail.

2. Mathematical Model. We consider a two-dimensional thin strip of length $L > 0$, which is axisymmetric at $\hat{\Gamma}_{\text{sym}} := [0, L] \times \{0\}$. Let $\hat{w} : [0, L] \to (0, \infty)$ be a given smooth function (which is bounded away from zero), that describes the wall $\hat{\Gamma}_{\text{w}} := \{\hat{\boldsymbol{x}} \in (0, L) \times (0, \infty) \mid \hat{x}_2 = \hat{w}(\hat{x}_1)\}$. Here and in the following, the subscripts $\cdot_1$ and $\cdot_2$ denote the components of a vector. Then the domain of interest is $\hat{\Omega} := \{\hat{\boldsymbol{x}} \in (0, L) \times (0, \infty) \mid \hat{x}_2 < \hat{w}(\hat{x}_1)\}$. At each time $\hat{t} \in [0, \infty)$, the domain is partitioned into two subdomains $\hat{\Omega}_{\text{I}}(\hat{t})$ and $\hat{\Omega}_{\text{II}}(\hat{t})$, which represent the parts occupied by the two fluids; one at the inlet boundary $\hat{\Gamma}_{\text{in}} := \{0\} \times [0, \hat{w}(0)]$ and the other at the outflow boundary $\hat{\Gamma}_{\text{out}} := \{L\} \times [0, \hat{w}(L)]$. For an illustration of the geometry,
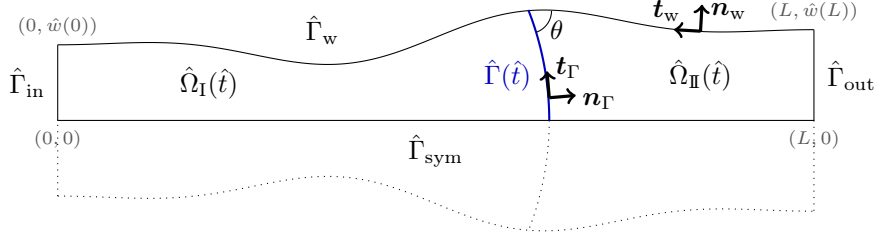
FIGURE 2.1. *Sketch of the half thin strip $\hat{\Omega}$ filled by two fluids with interface $\hat{\Gamma}(\hat{t})$ at time $\hat{t}$.*

see Figure 2.1.

We consider the particular case when the two fluids are separated by an axisymmetric fluid-fluid interface $\hat{\Gamma}(\hat{t}) := \partial\hat{\Omega}_{\mathrm{I}}(\hat{t}) \cap \partial\hat{\Omega}_{\mathbb{II}}(\hat{t})$, which is in contact with the solid wall $\hat{\Gamma}_{\mathrm{w}}$. This interface has an a-priori unknown location and shape, and therefore appears as a free boundary in the mathematical model. It is parametrized by $\hat{\boldsymbol{\gamma}} : [0, \infty) \times [0, 1] \to \overline{\hat{\Omega}}$, such that $\hat{\Gamma}(\hat{t}) = \{\hat{\boldsymbol{\gamma}}(\hat{t}, s) \mid s \in [0, 1]\}$. The parametrization starts at the symmetry boundary and ends at the wall, i.e.,

$$(2.1) \qquad \hat{\gamma}_2(\hat{t}, 0) = 0, \qquad\qquad \hat{\gamma}_2(\hat{t}, 1) = \hat{w}(\hat{\gamma}_1(\hat{t}, 1)).$$

The point $\hat{\boldsymbol{x}}^*(\hat{t}) := \hat{\boldsymbol{\gamma}}(\hat{t}, 1)$ is the so-called contact point.

At all boundaries of $\hat{\Omega}$, the outward normal and tangential unit vectors are denoted $\boldsymbol{n}$ and $\boldsymbol{t}$ with an index specifying the part of the boundary, e.g. $\boldsymbol{n}_{\mathrm{sym}}$ for the normal vector at the symmetry boundary $\hat{\Gamma}_{\mathrm{sym}}$. At the fluid-fluid interface $\hat{\Gamma}(\hat{t})$, the normal unit vector pointing from $\hat{\Omega}_{\mathrm{I}}(\hat{t})$ into $\hat{\Omega}_{\mathbb{II}}(\hat{t})$ is denoted by $\boldsymbol{n}_{\Gamma}$, while the tangential unit vector is $\boldsymbol{t}_{\Gamma}$. Therefore, these vectors are given by

$$\boldsymbol{t}_{\Gamma} = \frac{\partial_s \hat{\boldsymbol{\gamma}}}{|\partial_s \hat{\boldsymbol{\gamma}}|} = \frac{1}{\sqrt{(\partial_s \hat{\gamma}_1)^2 + (\partial_s \hat{\gamma}_2)^2}} \partial_s \hat{\boldsymbol{\gamma}}, \qquad \boldsymbol{n}_{\Gamma} = \frac{\partial_s \boldsymbol{t}_{\Gamma}}{|\partial_s \boldsymbol{t}_{\Gamma}|} = \frac{1}{\sqrt{(\partial_s \hat{\gamma}_1)^2 + (\partial_s \hat{\gamma}_2)^2}} \begin{pmatrix} \partial_s \hat{\gamma}_2 \\ -\partial_s \hat{\gamma}_1 \end{pmatrix},$$

$$\boldsymbol{t}_{\mathrm{w}} = -\frac{1}{\sqrt{1 + (\partial_{\hat{x}_1} \hat{w})^2}} \begin{pmatrix} 1 \\ \partial_{\hat{x}_1} \hat{w} \end{pmatrix}, \qquad\qquad \boldsymbol{n}_{\mathrm{w}} = \frac{1}{\sqrt{1 + (\partial_{\hat{x}_1} \hat{w})^2}} \begin{pmatrix} -\partial_{\hat{x}_1} \hat{w} \\ 1 \end{pmatrix},$$

$$\boldsymbol{t}_{\mathrm{sym}} = \begin{pmatrix} 1 \\ 0 \end{pmatrix}, \qquad\qquad \boldsymbol{n}_{\mathrm{sym}} = \begin{pmatrix} 0 \\ -1 \end{pmatrix},$$

$$\boldsymbol{t}_{\mathrm{in}} = \begin{pmatrix} 0 \\ -1 \end{pmatrix}, \qquad\qquad \boldsymbol{n}_{\mathrm{in}} = \begin{pmatrix} -1 \\ 0 \end{pmatrix},$$

$$\boldsymbol{t}_{\mathrm{out}} = \begin{pmatrix} 0 \\ 1 \end{pmatrix}, \qquad\qquad \boldsymbol{n}_{\mathrm{out}} = \begin{pmatrix} 1 \\ 0 \end{pmatrix}.$$

In each sub-domain $\hat{\Omega}_m(\hat{t})$, $m \in \{\mathrm{I}, \mathbb{II}\}$, we assume that the flow is modelled by the incompressible Navier-Stokes equations, which are written in dimensional form

$$(2.2) \qquad \rho_m\big(\partial_{\hat{t}}\hat{\boldsymbol{u}}_m + (\hat{\boldsymbol{u}}_m \cdot \hat{\nabla})\hat{\boldsymbol{u}}_m\big) + \hat{\nabla}\hat{p}_m = \mu_m \hat{\Delta}\hat{\boldsymbol{u}}_m \qquad\qquad \text{in } \hat{\Omega}_m(\hat{t}),$$

$$(2.3) \qquad \hat{\nabla}\cdot\hat{\boldsymbol{u}}_m = 0 \qquad\qquad \text{in } \hat{\Omega}_m(\hat{t}),$$

where $\hat{\boldsymbol{u}}_m(\hat{t}, \hat{\boldsymbol{x}})$ and $\hat{p}_m(\hat{t}, \hat{\boldsymbol{x}})$ are the velocity and pressure of fluid m. The parameters ρ_m and μ_m denote the density and the dynamic viscosity of the fluid. The symmetry conditions at $\hat{\Gamma}_{\mathrm{sym},m}(\hat{t}) := \hat{\Gamma}_{\mathrm{sym}} \cap \partial\hat{\Omega}_m(\hat{t})$ are

$$(2.4) \qquad \hat{\boldsymbol{u}}_m \cdot \boldsymbol{n}_{\mathrm{sym}} = 0, \qquad \boldsymbol{t}_{\mathrm{sym}} \cdot \big(\hat{\nabla}\hat{\boldsymbol{u}}_m \boldsymbol{n}_{\mathrm{sym}}\big) = 0 \qquad\qquad \text{on } \hat{\Gamma}_{\mathrm{sym},m}(\hat{t}),$$

$$(2.5) \qquad \hat{\nabla}\hat{p}_m \cdot \boldsymbol{n}_{\mathrm{sym}} = 0 \qquad\qquad \text{on } \hat{\Gamma}_{\mathrm{sym},m}(\hat{t}),$$

$$(2.6) \qquad \boldsymbol{n}_{\Gamma} \cdot \boldsymbol{n}_{\mathrm{sym}} = 0 \qquad\qquad \text{at } s = 0.$$

The walls $\hat{\Gamma}_{w,m}(\hat{t}) := \hat{\Gamma}_w \cap \partial\hat{\Omega}_m(\hat{t})$ in contact with fluid $m \in \{I, II\}$ are assumed impermeable, such that there is no fluid flow in normal direction, i.e.,

$$(2.7) \qquad \hat{\boldsymbol{u}}_m \cdot \boldsymbol{n}_w = 0 \qquad\qquad \text{on } \hat{\Gamma}_{w,m}(\hat{t}).$$

Traditionally, this is complemented with the no-slip condition $\hat{\boldsymbol{u}}_m \cdot \boldsymbol{t}_w = 0$ under the assumption that the fluid adheres to the wall. However, the no-slip condition leads to a singularity in the pressure and in the shear stress at the contact point $\hat{\boldsymbol{x}}^*(t)$ between wall $\hat{\Gamma}_w$ and interface $\hat{\Gamma}(\hat{t})$ [39, 23, 22]. To overcome this issue, several alternative boundary conditions have been proposed for use close to the contact point (or contact line in three dimensions), see [57, 12, 65] and the references therein. Here, we consider the Navier-slip condition

$$(2.8) \qquad \boldsymbol{t}_w \cdot \left(\hat{\boldsymbol{u}}_m + 2\hat{\lambda}\hat{\mathbf{D}}(\hat{\boldsymbol{u}}_m)\boldsymbol{n}_w\right) = 0 \qquad\qquad \text{on } \hat{\Gamma}_{w,m}(\hat{t}),$$

where $\hat{\mathbf{D}}(\hat{\boldsymbol{u}}) := \frac{1}{2}(\hat{\nabla}\hat{\boldsymbol{u}} + (\hat{\nabla}\hat{\boldsymbol{u}})^T)$ denotes the symmetric strain and $\hat{\lambda}$ is the slip length. This condition has been proposed originally by Huh and Scriven [39] to resolve the contact-line problem, and has been frequently used [35, 38, 19, 27, 63, 58]. Often, the Navier slip condition is only applied close to the contact point. In this case, a variable slip length $\hat{\lambda}(\hat{x}_1)$ is adopted, decaying rapidly to zero away from the contact point $\hat{\boldsymbol{x}}^*(\hat{t})$, see e.g. [25, 16, 27, 4]. This seems justified by molecular dynamics simulations showing that the no-slip boundary condition is only violated in a small region (up to some nm) around the contact point [43, 44, 68, 67, 42]. Additionally, surface wettability and roughness strongly affect the slip behaviour, see e.g. [40, 47, 5, 26] for a mathematical analysis.

Remark 2.1. To be general, we will consider two cases here: a constant slip length $\hat{\lambda}$ on the whole wall $\hat{\Gamma}_w$, or a varying slip length $\hat{\lambda}(\hat{t}, \hat{x}_1) = \hat{\lambda}_0 \exp(-c|\hat{x}_1 - \hat{x}_1^*(\hat{t})|)$ which decreases exponentially away from the contact point $\hat{\boldsymbol{x}}^*(\hat{t})$. Note that the overall dynamics of the two-phase system will be independent of the latter, local slip condition, and especially of the exact form used; only the flow field close to the interface will be affected, see section 3. This is in accordance with the results in [22, 63]. Furthermore, for smooth solutions the continuity of the fluid velocities (2.10) across the interface $\hat{\Gamma}(\hat{t})$ and the Navier slip condition (2.8) at the wall $\hat{\Gamma}_{w,m}(\hat{t})$ only holds, if the slip length $\hat{\lambda}$ at the contact point $\hat{\boldsymbol{x}}^*(\hat{t})$ is the same in both fluids. Therefore, we consider the same slip length $\hat{\lambda}$ for both fluids, although they could in principle differ.

At the contact point $\hat{\boldsymbol{x}}^*(t)$, the contact angle θ between the wall $\hat{\Gamma}_w(\hat{t})$ and the fluid interface $\hat{\Gamma}(\hat{t})$ must be prescribed. Minimization of the total surface energy yields the well-known Young's relation $\sigma_I - \sigma_{II} = \sigma \cos\theta_s$, where σ_I and σ_{II} denote the surface tension coefficients between the solid and the two fluids, and σ the interfacial tension between the two fluids. The angle θ_s is called the static contact angle and measured from the side of fluid II, as shown in Figure 2.1. Experiments performed under dynamic conditions show a dynamic behaviour of the contact angle. This is expressed as an apparent contact angle θ, and has a major influence on the overall flow dynamics [10]. In general, observations show increasing advancing angles, but decreasing receding angles, when the contact-line velocity U increases [22, 9]. The θ-U relation is essentially monotonic.

There are mainly two models to describe this phenomenon: the hydrodynamic theory and the molecular kinetic theory, for detailed reviews see [10, 56, 12]. The hydrodynamic theory emphasises on dissipation due to viscous flow within the wedge

of liquid near the moving contact line. The region close to the contact point is analysed based on asymptotic expansions [35, 72, 37, 22, 19, 16]. For two-phase flow this yields the well-known Cox law $g(\theta) = g(\theta_s) + C\mu U/\sigma$ for the dynamic contact angle θ, where U denotes the contact line velocity, the constant C depends on the specific slip model, and g is an analytically derived function, which can be approximated by $g(\theta) \approx \theta^3$ for small angles [16]. The other approach is the molecular kinetic theory, where the dissipation is described due to the dynamic friction associated with the moving contact line. This yields the relation $U = C_1 \sinh(C_2\sigma(\cos\theta_s - \cos\theta))$ with the constants C_1 and C_2 depending on molecular properties [11, 15, 9]. After linearisation for small differences in the angles, one obtains $U = C\sigma(\cos\theta_s - \cos\theta)$ for some constant C [10].

As for the slip length, the contact angle is strongly affected by surface wettability and roughness. In [10, 56], the resulting effects are made responsible for contact angle hysteresis, i.e., that static contact angles can be achieved in the whole range $\theta_r < \theta_s < \theta_a$, where θ_a, θ_r denote the advancing and receding contact angles, respectively. Summarizing all the above results, we assume the contact angle θ to depend on the velocity $-\partial_t\hat{\boldsymbol{x}}^*(t) \cdot \boldsymbol{t}_{\mathrm{w}}$ of the contact point parallel to the wall. Recall that $\hat{\boldsymbol{x}}^* = \hat{\boldsymbol{\gamma}}|_{s=1}$, so this contact angle condition is expressed as

$$(2.9) \qquad \cos(\theta(-\partial_t\hat{\boldsymbol{\gamma}} \cdot \boldsymbol{t}_{\mathrm{w}}|_{\hat{x}_1 = \hat{\gamma}_1})) = \boldsymbol{t}_\Gamma \cdot \boldsymbol{t}_{\mathrm{w}}\big|_{\hat{x}_1 = \hat{\gamma}_1} \qquad\qquad \text{at } s = 1,$$

where $\theta : \mathbb{R} \to (0, \pi)$ is a given dynamic contact angle model. Note that any dynamic contact angle model that satisfies assumption (A5) below can be used. Specific relations for hysteretic θ and their effect on the behaviour will be discussed in subsection 3.4. Furthermore, to account for heterogeneities, the following analysis can be straightforwardly extended to the case when the contact angle also depends on the position $\hat{x}_1^*(t)$ of the contact point.

At the interface $\hat{\Gamma}(\hat{t})$, there holds continuity of the velocity and of the tangential stress, while the jump in the normal stress is caused by the surface tension

$$(2.10) \qquad\qquad\qquad\qquad\qquad\qquad\qquad \hat{\boldsymbol{u}}_{\mathrm{I}} = \hat{\boldsymbol{u}}_{\mathrm{II}} \qquad\qquad \text{on } \hat{\Gamma}(\hat{t}),$$

$$(2.11) \qquad -(\hat{p}_{\mathrm{I}} - \hat{p}_{\mathrm{II}})\boldsymbol{n}_\Gamma + 2\big(\mu_{\mathrm{I}}\hat{\mathbf{D}}(\hat{\boldsymbol{u}}_{\mathrm{I}}) - \mu_{\mathrm{II}}\hat{\mathbf{D}}(\hat{\boldsymbol{u}}_{\mathrm{II}})\big)\boldsymbol{n}_\Gamma = \sigma\hat{\kappa}\boldsymbol{n}_\Gamma \qquad \text{on } \hat{\Gamma}(\hat{t}),$$

where $\hat{\kappa} = \frac{\det(\partial_s\boldsymbol{\gamma}, \partial_s^2\boldsymbol{\gamma})}{|\partial_s\boldsymbol{\gamma}|^3}$ is the local mean curvature of the interface. Note that this curvature generalizes to $\hat{\nabla} \cdot \boldsymbol{n}_\Gamma$ for three-dimensional domains. The interface moves according to the normal velocity of the fluids,

$$(2.12) \qquad \partial_{\hat{t}}\hat{\boldsymbol{\gamma}} \cdot \boldsymbol{n}_\Gamma = \hat{\boldsymbol{u}}_{\mathrm{I}} \cdot \boldsymbol{n}_\Gamma \qquad\qquad\qquad\qquad\qquad \text{on } \hat{\Gamma}(\hat{t}).$$

At the inlet boundary $\hat{\Gamma}_{\mathrm{in}}$, either the pressure $\hat{p}_{\mathrm{in}}$ or the velocity $\hat{\boldsymbol{u}}_{\mathrm{in}}$ is given, namely either

$$(2.13) \qquad\qquad \hat{p}_{\mathrm{I}} = \hat{p}_{\mathrm{in}}, \quad \hat{\boldsymbol{u}}_{\mathrm{I}} \cdot \boldsymbol{t}_{\mathrm{in}} = 0 \qquad \text{or} \qquad \hat{\boldsymbol{u}}_{\mathrm{I}} = \hat{\boldsymbol{u}}_{\mathrm{in}} \qquad\qquad \text{on } \hat{\Gamma}_{\mathrm{in}},$$

while an outflow boundary condition is applied at $\hat{\Gamma}_{\mathrm{out}}$ (corresponding to $\hat{p}_{\mathrm{out}} = 0$)

$$(2.14) \qquad\qquad \hat{p}_{\mathrm{II}} = 0, \quad \hat{\boldsymbol{u}}_{\mathrm{II}} \cdot \boldsymbol{t}_{\mathrm{out}} = 0 \qquad\qquad\qquad\qquad \text{on } \hat{\Gamma}_{\mathrm{out}}.$$

The problem is closed by the initial conditions $\hat{\boldsymbol{\gamma}}|_{\hat{t}=0} = \hat{\boldsymbol{\gamma}}_0$ for the position of the interface $\hat{\Gamma}(0)$ and $\hat{\boldsymbol{u}}_m|_{\hat{t}=0} = \hat{\boldsymbol{u}}_{m,0}$ for the velocity in $\hat{\Omega}_m(0)$. In the following, we will omit the initial conditions and implicitly require them to match the asymptotic solutions in section 3 to avoid possible initial layer solutions for small times.

2.1. Dimensionless Formulation. To quantify the importance of the different terms of the model, we rewrite the equations in a dimensionless form. As we consider a single, thin pore, we introduce the small parameter $\varepsilon = \hat{w}(0)/L \ll 1$ which characterizes the ratio of the typical width to the length of the thin strip. Note that in a general porous medium, ε would reflect the ratio of the size of a pore to the length scale of a representative elementary volume. With this, we rescale the governing equations using the dimensionless quantities

$$x_1 := \tfrac{\hat{x}_1}{L}, \quad x_2 := \tfrac{\hat{x}_2}{\hat{w}(0)} = \tfrac{\hat{x}_2}{\varepsilon L}, \quad t := \tfrac{\hat{t}U}{L}, \quad \lambda^\varepsilon := \tfrac{\hat{\lambda}}{\hat{w}(0)} = \tfrac{\hat{\lambda}}{\varepsilon L},$$

$$\gamma_1^\varepsilon(t,s) := \tfrac{\hat{\gamma}_1(\hat{t},s)}{L}, \quad \gamma_2^\varepsilon(t,s) := \tfrac{\hat{\gamma}_2(\hat{t},s)}{\hat{w}(0)} = \tfrac{\hat{\gamma}_2(\hat{t},s)}{\varepsilon L}, \quad w^\varepsilon(x_1) := \tfrac{\hat{w}(\hat{x}_1)}{\hat{w}(0)} = \tfrac{\hat{w}(\hat{x}_1)}{\varepsilon L},$$

$$\theta^\varepsilon(v) := \theta(vU), \quad \boldsymbol{u}_m^\varepsilon(t,\boldsymbol{x}) := \tfrac{\hat{\boldsymbol{u}}_m(\hat{t},\hat{\boldsymbol{x}})}{U}, \quad p_m^\varepsilon(t,\boldsymbol{x}) := \tfrac{\hat{p}_m(\hat{t},\hat{\boldsymbol{x}})\varepsilon^2 L}{\mu_{\mathrm{I}}U},$$

where $U > 0$ denotes a characteristic velocity. In particular, the pressure reference $\mu_{\mathrm{I}}U/(\varepsilon^2 L)$ is chosen such that pressure and viscous stress terms in (2.2) are balanced. For moderate Reynolds number, this choice ensures laminar flow driven by the pressure gradients, which is crucial for the validity of Darcy's law on the Darcy scale. Note that the coordinates x_1 and x_2 are scaled differently to obtain a domain of order 1, $\mathcal{O}(\varepsilon^0)$. Hence, the non-dimensional differential operators are

$$\nabla^\varepsilon = \begin{pmatrix} \partial_{x_1} \\ \varepsilon^{-1}\partial_{x_2} \end{pmatrix}, \qquad\qquad \Delta^\varepsilon = \partial_{x_1}^2 + \varepsilon^{-2}\partial_{x_2}^2,$$

and the divergence changes accordingly. The non-dimensional domains and boundaries become

$$\Gamma^\varepsilon(t) = \{\boldsymbol{\gamma}^\varepsilon(t,s) \mid s \in [0,1]\}, \quad \Omega^\varepsilon = \{\boldsymbol{x} \in (0,1)\times(0,\infty) \mid x_2 < w^\varepsilon(x_1)\},$$

$$\Gamma_{\mathrm{in}}^\varepsilon = \{0\}\times[0,1], \quad \mathcal{M} := \{O \subset \Omega^\varepsilon \setminus \Gamma^\varepsilon(t) \mid O \cup \Gamma_{\mathrm{in}}^\varepsilon \text{ is connected}\},$$

$$\Omega_{\mathrm{I}}^\varepsilon(t) = \bigcup_{O\in\mathcal{M}} O, \quad \Omega_{\mathrm{II}}^\varepsilon(t) = \Omega^\varepsilon \setminus (\Gamma^\varepsilon(t) \cup \Omega_{\mathrm{I}}^\varepsilon(t)), \quad \Gamma_{\mathrm{out}}^\varepsilon = \{1\}\times[0,w^\varepsilon(1)],$$

$$\Gamma_{\mathrm{sym},m}^\varepsilon(t) = \{\boldsymbol{x} \in \partial\Omega_m^\varepsilon(t) \mid x_2 = 0\}, \quad \Gamma_{\mathrm{w},m}^\varepsilon(t) = \{\boldsymbol{x} \in \partial\Omega_m^\varepsilon(t) \mid x_2 = w^\varepsilon(x_1)\}.$$

After the rescaling of (2.1)–(2.14), the dimensionless equations read

$$(2.15) \qquad \varepsilon^2\mathrm{Re}\big(\partial_t\boldsymbol{u}_{\mathrm{I}}^\varepsilon + (\boldsymbol{u}_{\mathrm{I}}^\varepsilon\cdot\nabla^\varepsilon)\boldsymbol{u}_{\mathrm{I}}^\varepsilon\big) + \nabla^\varepsilon p_{\mathrm{I}}^\varepsilon = \varepsilon^2\,\Delta^\varepsilon\boldsymbol{u}_{\mathrm{I}}^\varepsilon \qquad \text{in } \Omega_{\mathrm{I}}^\varepsilon(t),$$

$$(2.16) \qquad \varepsilon^2\mathrm{RRe}\big(\partial_t\boldsymbol{u}_{\mathrm{II}}^\varepsilon + (\boldsymbol{u}_{\mathrm{II}}^\varepsilon\cdot\nabla^\varepsilon)\boldsymbol{u}_{\mathrm{II}}^\varepsilon\big) + \nabla^\varepsilon p_{\mathrm{II}}^\varepsilon = \mathrm{M}\varepsilon^2\,\Delta^\varepsilon\boldsymbol{u}_{\mathrm{II}}^\varepsilon \qquad \text{in } \Omega_{\mathrm{II}}^\varepsilon(t),$$

$$(2.17) \qquad \nabla^\varepsilon\cdot\boldsymbol{u}_m^\varepsilon = 0 \qquad \text{in } \Omega_m^\varepsilon(t),$$

$$(2.18) \qquad \boldsymbol{u}_m^\varepsilon\cdot\boldsymbol{n}_{\mathrm{sym}} = 0, \quad \boldsymbol{t}_{\mathrm{sym}}\cdot(\nabla^\varepsilon\boldsymbol{u}_m^\varepsilon\boldsymbol{n}_{\mathrm{sym}}) = 0 \qquad \text{on } \Gamma_{\mathrm{sym},m}^\varepsilon(t),$$

$$(2.19) \qquad \nabla^\varepsilon p_m^\varepsilon\cdot\boldsymbol{n}_{\mathrm{sym}} = 0, \qquad \text{on } \Gamma_{\mathrm{sym},m}^\varepsilon(t),$$

$$(2.20) \quad \text{either} \quad p_{\mathrm{I}}^\varepsilon = p_{\mathrm{in}}^\varepsilon, \quad \boldsymbol{u}_{\mathrm{I}}^\varepsilon\cdot\boldsymbol{t}_{\mathrm{in}} = 0, \qquad \text{or} \qquad \boldsymbol{u}_{\mathrm{I}}^\varepsilon = \boldsymbol{u}_{\mathrm{in}}^\varepsilon \qquad \text{on } \Gamma_{\mathrm{in}}^\varepsilon,$$

$$(2.21) \qquad p_{\mathrm{II}}^\varepsilon = 0, \quad \boldsymbol{u}_{\mathrm{II}}^\varepsilon\cdot\boldsymbol{t}_{\mathrm{out}} = 0 \qquad \text{on } \Gamma_{\mathrm{out}}^\varepsilon,$$

$$(2.22) \qquad \boldsymbol{t}_{\mathrm{w}}^\varepsilon\cdot(\boldsymbol{u}_m^\varepsilon + 2\varepsilon\lambda^\varepsilon\mathbf{D}^\varepsilon(\boldsymbol{u}_m^\varepsilon)\boldsymbol{n}_{\mathrm{w}}^\varepsilon) = 0, \quad \boldsymbol{u}_m^\varepsilon\cdot\boldsymbol{n}_{\mathrm{w}}^\varepsilon = 0 \qquad \text{on } \Gamma_{\mathrm{w},m}^\varepsilon(t),$$

$$(2.23) \qquad \partial_t\begin{pmatrix}\gamma_1^\varepsilon \\ \varepsilon\gamma_2^\varepsilon\end{pmatrix}\cdot\boldsymbol{n}_\Gamma^\varepsilon = \boldsymbol{u}_{\mathrm{I}}^\varepsilon\cdot\boldsymbol{n}_\Gamma^\varepsilon, \quad \boldsymbol{u}_{\mathrm{I}}^\varepsilon = \boldsymbol{u}_{\mathrm{II}}^\varepsilon \qquad \text{on } \Gamma^\varepsilon(t),$$

$$(2.24) \qquad -(p_{\mathrm{I}}^\varepsilon - p_{\mathrm{II}}^\varepsilon)\boldsymbol{n}_\Gamma^\varepsilon + 2\varepsilon^2\big(\mathbf{D}^\varepsilon(\boldsymbol{u}_{\mathrm{I}}^\varepsilon) - \mathrm{M}\,\mathbf{D}^\varepsilon(\boldsymbol{u}_{\mathrm{II}}^\varepsilon)\big)\boldsymbol{n}_\Gamma^\varepsilon = \tfrac{\varepsilon^2}{\mathrm{Ca}}\kappa^\varepsilon\boldsymbol{n}_\Gamma^\varepsilon \qquad \text{on } \Gamma^\varepsilon(t),$$

$$(2.25) \qquad \boldsymbol{n}_\Gamma^\varepsilon\cdot\boldsymbol{n}_{\mathrm{sym}} = 0 \qquad \text{at } s = 0,$$

$$(2.26) \qquad \cos(\theta^\varepsilon(-\partial_t\boldsymbol{\gamma}^\varepsilon\cdot\boldsymbol{t}_{\mathrm{w}}^\varepsilon|_{x_1=\gamma_1^\varepsilon})) = \boldsymbol{t}_\Gamma^\varepsilon\cdot\boldsymbol{t}_{\mathrm{w}}^\varepsilon\big|_{x_1=\gamma_1^\varepsilon} \qquad \text{at } s = 1,$$

for $m \in \{\mathrm{I}, \mathrm{I\!I}\}$, where

$$\mathrm{Re} = \frac{\rho_\mathrm{I} U L}{\mu_\mathrm{I}} > 0, \qquad \mathrm{Ca} = \frac{\mu_\mathrm{I} U}{\sigma} > 0, \qquad \mathrm{M} = \frac{\mu_\mathrm{I\!I}}{\mu_\mathrm{I}} > 0 \qquad \text{and} \qquad \mathrm{R} = \frac{\rho_\mathrm{I\!I}}{\rho_\mathrm{I}} > 0$$

denote the effective Reynolds number, the capillary number and the viscosity and density ratio, respectively.

The non-dimensional strain is given by $\mathbf{D}^\varepsilon(\boldsymbol{u}^\varepsilon) = \frac{1}{2}(\nabla^\varepsilon \boldsymbol{u}^\varepsilon + (\nabla^\varepsilon \boldsymbol{u}^\varepsilon)^T)$ and the transformed normal and tangential vectors are

$$\boldsymbol{t}_\mathrm{w}^\varepsilon = -\frac{1}{\sqrt{1+\varepsilon^2(\partial_{x_1} w^\varepsilon)^2}}\begin{pmatrix} 1 \\ \varepsilon\partial_{x_1} w^\varepsilon \end{pmatrix}, \qquad\qquad \boldsymbol{n}_\mathrm{w}^\varepsilon = \frac{1}{\sqrt{1+\varepsilon^2(\partial_{x_1} w^\varepsilon)^2}}\begin{pmatrix} -\varepsilon\partial_{x_1} w^\varepsilon \\ 1 \end{pmatrix},$$

$$\boldsymbol{t}_\Gamma^\varepsilon = \frac{1}{\sqrt{(\partial_s\gamma_1^\varepsilon)^2+\varepsilon^2(\partial_s\gamma_2^\varepsilon)^2}}\begin{pmatrix} \partial_s\gamma_1^\varepsilon \\ \varepsilon\partial_s\gamma_2^\varepsilon \end{pmatrix}, \qquad \boldsymbol{n}_\Gamma^\varepsilon = \frac{1}{\sqrt{(\partial_s\gamma_1^\varepsilon)^2+\varepsilon^2(\partial_s\gamma_2^\varepsilon)^2}}\begin{pmatrix} \varepsilon\partial_s\gamma_2^\varepsilon \\ -\partial_s\gamma_1^\varepsilon \end{pmatrix}.$$

Furthermore, the non-dimensional curvature is given by

$$\kappa^\varepsilon = \frac{\varepsilon\det(\partial_s\boldsymbol{\gamma}^\varepsilon, \partial_s^2\boldsymbol{\gamma}^\varepsilon)}{\left((\partial_s\gamma_1^\varepsilon)^2+\varepsilon^2(\partial_s\gamma_2^\varepsilon)^2\right)^{3/2}} = \frac{\varepsilon\left(\partial_s\gamma_1^\varepsilon\partial_s^2\gamma_2^\varepsilon - \partial_s\gamma_2^\varepsilon\partial_s^2\gamma_1^\varepsilon\right)}{\left((\partial_s\gamma_1^\varepsilon)^2+\varepsilon^2(\partial_s\gamma_2^\varepsilon)^2\right)^{3/2}}.$$

Remark 2.2. Integrating (2.17) for $m = \mathrm{I}$ over $V_a = \{\boldsymbol{x} \in \Omega_\mathrm{I}^\varepsilon(t) \mid x_1 < a\}$ for any $a < \min_{s\in[0,1]} \gamma_1^\varepsilon(t,s)$ yields by the Gauss theorem and the boundary conditions (2.18) and (2.22)

$$0 = \int_{V_a} \nabla^\varepsilon \cdot \boldsymbol{u}_\mathrm{I}^\varepsilon d\boldsymbol{x} = \int_{\partial V_a} \boldsymbol{u}_\mathrm{I}^\varepsilon \cdot \boldsymbol{n} ds = \int_0^{w^\varepsilon(a)} u_{\mathrm{I},1}^\varepsilon\big|_{x_1=a} dx_2 - \int_0^1 u_{\mathrm{I},1}^\varepsilon\big|_{x_1=0} dx_2.$$

Denoting the total flux into the half strip by $q^\varepsilon(t,0) := \int_0^1 u_{\mathrm{I},1}^\varepsilon(t,\boldsymbol{x})\big|_{x_1=0} dx_2$, we obtain that for all $a < \min_{s\in[0,1]} \gamma_1^\varepsilon(t,s)$ the total flux $q^\varepsilon(t,a) := \int_0^{w^\varepsilon(a)} u_{\mathrm{I},1}^\varepsilon\big|_{x_1=a} dx_2 = q^\varepsilon(t,0)$. Analogously, integrating (2.17) for $m = \mathrm{I}$ over $\Omega_\mathrm{I}^\varepsilon(t)$ and for $m = \mathrm{I\!I}$ over $V_a = \{\boldsymbol{x} \in \Omega_\mathrm{I\!I}^\varepsilon \mid x_1 < a\}$ for any $a > \max_{s\in[0,1]} \gamma_1^\varepsilon(t,s)$ yields by the Gauss theorem, the boundary conditions (2.18) and (2.22) and the continuity of velocity at the interface (2.23) that

$$0 = \int_{\Omega_\mathrm{I}^\varepsilon} \nabla^\varepsilon \cdot \boldsymbol{u}_\mathrm{I}^\varepsilon d\boldsymbol{x} + \int_{V_a} \nabla^\varepsilon \cdot \boldsymbol{u}_\mathrm{I\!I}^\varepsilon d\boldsymbol{x} = -q^\varepsilon(t,0) + \int_0^{w^\varepsilon(a)} u_{\mathrm{I\!I},1}^\varepsilon\big|_{x_1=a} dx_2,$$

i.e., the total flux $q(t,a) := \int_0^{w^\varepsilon(a)} u_{\mathrm{I\!I},1}^\varepsilon\big|_{x_1=a} dx_2 = q^\varepsilon(t,0)$ for all $a > \max_{s\in[0,1]} \gamma_1^\varepsilon(t,s)$. Within the interval $[\min_{s\in[0,1]} \gamma_1^\varepsilon(t,s), \max_{s\in[0,1]} \gamma_1^\varepsilon(t,s)]$, the same calculation shows that the sum of the two fluxes over the respective parts of the domain equals the total flux $q^\varepsilon(t,0)$. This means that the total flux is independent of x_1, so we will simply use $q^\varepsilon(t)$ in this result for the subsequent analysis.

3. Asymptotic Expansions. In this section, we derive the formal solution for the two-phase flow system (2.15)–(2.26) in the asymptotic limit as $\varepsilon \to 0$, i.e., the behaviour in the limit when the thin strip becomes infinitely thin. We start with the solution in the bulk domains $\Omega_m^\varepsilon(t)$, $m \in \{\mathrm{I}, \mathrm{I\!I}\}$, away from the interface $\Gamma^\varepsilon(t)$, where either fluid I or $\mathrm{I\!I}$ is present, respectively. In the subsequent section, we show that these bulk solutions are connected via a boundary layer solution in the vicinity of $\Gamma^\varepsilon(t)$. Altogether, the solution is of Hagen-Poiseuille type in the bulk coupled by a dynamic Young-Laplace law at the interface, such that the interface position and the total flux are given by differential algebraic equations. Furthermore, we show that the solution for vanishing viscosity ratio $\mathrm{M} \to 0$ matches the asymptotic limit

for unsaturated one-phase flow. Finally, a reformulation for hysteretic contact angle models is discussed.

For the following analysis we use an asymptotic expansion technique with respect to ε to derive effective models. All variables are assumed to be smooth and to depend regularly on ε starting with the leading order $\mathcal{O}(\varepsilon^0)$. We apply the homogenization ansatz

$$\boldsymbol{u}_m^\varepsilon(t,\boldsymbol{x}) = \boldsymbol{u}_m^0(t,\boldsymbol{x}) + \varepsilon\boldsymbol{u}_m^1(t,\boldsymbol{x}) + \mathcal{O}(\varepsilon^2),$$
$$p_m^\varepsilon(t,\boldsymbol{x}) = p_m^0(t,\boldsymbol{x}) + \varepsilon p_m^1(t,\boldsymbol{x}) + \mathcal{O}(\varepsilon^2),$$
$$\boldsymbol{\gamma}^\varepsilon(t,s) = \boldsymbol{\gamma}^0(t,s) + \varepsilon\boldsymbol{\gamma}^1(t,s) + \mathcal{O}(\varepsilon^2),$$

for $m \in \{\mathrm{I}, \mathrm{I\!I}\}$. Inserting the asymptotic expansions into the two-phase flow equations (2.15)–(2.26) and equating terms of the same order in ε, we will obtain the asymptotic equations and solutions in the limit as $\varepsilon \to 0$. To this end, we need some assumptions on the parameters of the model.

(A1) The Reynolds number Re and its product with the density ratio R are uniformly bounded for all $0 < \varepsilon \ll 1$, i.e., there exists $C \in (0,\infty)$ such that $\mathrm{Re} \leq C$ and $\mathrm{RRe} \leq C$ independent of ε. In other words $\mathrm{Re} = \mathcal{O}(\varepsilon^0)$ or $\mathrm{Re} = \mathrm{o}(\varepsilon^0)$, and $\mathrm{RRe} = \mathcal{O}(\varepsilon^0)$ or $\mathrm{RRe} = \mathrm{o}(\varepsilon^0)$.

(A2) The viscosity ratio M of the fluids is of order 1, $\mathrm{M} = \mathcal{O}(\varepsilon^0)$.

(A3) According to Remark 2.1, the slip length λ^ε has the form

$$\lambda^\varepsilon(t,x_1) = \lambda^0 + \lambda_e \exp\left(-\frac{|x_1 - x_1^*(t)|}{\varepsilon}\right),$$

for given constants $\lambda^0, \lambda_e \geq 0$ that are independent of ε. Moreover, there holds either $\lambda_e = 0$, or $\lambda^0 = 0$. Note that the latter represents the case of rapidly decaying slip away from the interface, so that λ^ε has the expansion $\lambda^\varepsilon(t,x_1) = \mathcal{O}(\varepsilon^N)$ for arbitrary $N \in \mathbb{N}$ as long as $x_1 - x_1^*(t) \gg \varepsilon$.

(A4) The wall function w^ε has a uniform expansion

$$w^\varepsilon(x_1) = w^0(x_1) + \varepsilon w^1(x_1) + \mathcal{O}(\varepsilon^2),$$

where $w^0 : [0,1] \to (0,\infty)$ is continuously differentiable (and thus bounded away from zero). Furthermore, there holds $\partial_{x_1} w^0(1) = \partial_{x_1} w^0(1) = 0$.

(A5) The contact angle relation θ^ε has a uniform expansion

$$\theta^\varepsilon(u) = \theta^0(u) + \varepsilon\theta^1(u) + \mathcal{O}(\varepsilon^2),$$

where $\theta^0 : \mathbb{R} \to (0,\pi)$ is Lipschitz-continuous.

(A6) If the velocity boundary condition $\boldsymbol{u}_\mathrm{I}^\varepsilon = \boldsymbol{u}_\mathrm{in}^\varepsilon$ is used at the inlet $\Gamma_\mathrm{in}^\varepsilon$, the velocity is given by

$$\boldsymbol{u}_\mathrm{in}^\varepsilon(t,\boldsymbol{x}) = \begin{pmatrix} 3q(t)\frac{(1+2\lambda^0)-x_2^2}{6\lambda^0+2} + \mathcal{O}(\varepsilon) \\ \mathcal{O}(\varepsilon^2) \end{pmatrix},$$

where $q : [0,\infty) \to \mathbb{R}$ is a continuous function independent of ε.

As will be seen below, (A1) ensures that the flow remains laminar. Furthermore, (A2) restricts the discussion to moderately viscous liquids. While $\mathrm{M} \gg 1$ would result in a highly viscous second fluid which gets immobile as $\varepsilon \to 0$, we will discuss the case $\mathrm{M} \ll 1$ of a extremely mobile fluid like air (compared to water or oil) separately

in subsection 3.3. The asymptotic expansion stated in (A4) and (A5) is crucial for
the derivation, while (A3) serves as a simplification to avoid technical complexity.
The main reason for a straight wall at inlet and outlet $(\partial_{x_1} w^0(1) = \partial_{x_1} w^0(1) = 0)$
together with (A6) is to avoid possible boundary layer effects. This can be relaxed if
the boundary conditions (2.20) and (2.21) at $\Gamma_{\text{in}}^\varepsilon$ and $\Gamma_{\text{out}}^\varepsilon$ are replaced appropriately.
Furthermore, rough walls of type $w^\varepsilon(x_1) = w^0(x_1) + \varepsilon w^1(x_1/\varepsilon) + \mathcal{O}(\varepsilon)$ would strongly
affect the shape and position of the interface. A naive extension of the following
results would yield unphysical oscillations of the interface, so that we restrict the
discussion to slowly varying walls.

Note that the normal and tangential vectors $\boldsymbol{n}_\Gamma^\varepsilon$, $\boldsymbol{t}_\Gamma^\varepsilon$, $\boldsymbol{n}_{\text{w}}^\varepsilon$ and $\boldsymbol{t}_{\text{w}}^\varepsilon$ depend on $\boldsymbol{\gamma}^\varepsilon$ and
w^ε, respectively, such that these can be expanded, e.g.

$$(3.1) \quad \boldsymbol{n}_{\text{w}}^\varepsilon = \begin{pmatrix} 0 \\ 1 \end{pmatrix} - \varepsilon \begin{pmatrix} \partial_{x_1} w^0 \\ 0 \end{pmatrix} + \mathcal{O}(\varepsilon^2),$$

$$(3.2) \quad \boldsymbol{n}_\Gamma^\varepsilon = \begin{cases} \begin{pmatrix} 0 \\ -\operatorname{sign}(\partial_s \gamma_1^0) \end{pmatrix} + \varepsilon \frac{1}{|\partial_s \gamma_1^0|} \begin{pmatrix} \partial_s \gamma_2^0 \\ -\partial_s \gamma_1^1 \end{pmatrix} + \mathcal{O}(\varepsilon^2) & \text{for } \partial_s \gamma_1^0 \neq 0, \\[2ex] \frac{1}{\sqrt{(\partial_s \gamma_1^1)^2 + (\partial_s \gamma_2^0)^2}} \begin{pmatrix} \partial_s \gamma_2^0 \\ -\partial_s \gamma_1^1 \end{pmatrix} + \varepsilon \frac{1}{\sqrt{(\partial_s \gamma_1^1)^2 + (\partial_s \gamma_2^0)^2}} \begin{pmatrix} \partial_s \gamma_2^1 \\ -\partial_s \gamma_1^1 \end{pmatrix} \\ \quad + \varepsilon \frac{\partial_s \gamma_1^1 \partial_s \gamma_1^2 + \partial_s \gamma_2^0 \partial_s \gamma_2^1}{((\partial_s \gamma_1^1)^2 + (\partial_s \gamma_2^0)^2)^{3/2}} \begin{pmatrix} -\partial_s \gamma_2^0 \\ \partial_s \gamma_1^1 \end{pmatrix} + \mathcal{O}(\varepsilon^2) & \text{otherwise.} \end{cases}$$

In particular, the direction of the normal vector $\boldsymbol{n}_\Gamma^\varepsilon$ depends on $\partial_s \gamma_1^0$. If $\partial_s \gamma_1^0 \neq 0$ for
some $s \in [0, 1]$, the interface $\Gamma^\varepsilon(t)$ is largely deformed over a region that has a width
$\mathcal{O}(\varepsilon^0)$, namely $I = [\min_{s \in [0,1]} \gamma_1^\varepsilon, \max_{s \in [0,1]} \gamma_1^\varepsilon]$ with $|I| = \mathcal{O}(\varepsilon^0)$. Therefore, there
are both fluids present along a transversal segment at any $x_1 \in I$, and complicated
interface dynamics occur in the limit $\varepsilon \to 0$. On the other hand, if $\partial_s \gamma_1^0 \equiv 0$, only
small deformations with $|I| = \mathcal{O}(\varepsilon)$ are possible, and we obtain asymptotically a sharp
transition from fluid I to fluid $\mathbb{II}$ at γ_1^0.

3.1. Flow in the bulk domains. First, we consider the flow in the bulk do-
mains Ω_m^ε, $m \in \{\text{I}, \mathbb{II}\}$, and solve the resulting equations away from the interface.
Inserting the homogenization ansatz into (2.15)–(2.22) using (A1)–(A6) and a Taylor
expansion around $x_2 = w^0(x_1)$ for (2.22), one obtains

$$(3.3) \qquad \mathcal{O}(\varepsilon) = \partial_{x_1} p_{\text{I}}^0 - \partial_{x_2}^2 u_{\text{I},1}^0 \qquad\qquad \text{in } \Omega_{\text{I}}^\varepsilon(t),$$

$$(3.4) \qquad \mathcal{O}(\varepsilon^0) = \varepsilon^{-1} \partial_{x_2} p_{\text{I}}^0 \qquad\qquad \text{in } \Omega_{\text{I}}^\varepsilon(t),$$

$$(3.5) \qquad \mathcal{O}(\varepsilon) = \partial_{x_1} p_{\mathbb{II}}^0 - \mathrm{M} \partial_{x_2}^2 u_{\mathbb{II},1}^0 \qquad\qquad \text{in } \Omega_{\mathbb{II}}^\varepsilon(t),$$

$$(3.6) \qquad \mathcal{O}(\varepsilon^0) = \varepsilon^{-1} \partial_{x_2} p_{\mathbb{II}}^0 \qquad\qquad \text{in } \Omega_{\mathbb{II}}^\varepsilon(t),$$

$$(3.7) \qquad \mathcal{O}(\varepsilon) = \varepsilon^{-1} \partial_{x_2} u_{m,2}^0 + \left(\partial_{x_1} u_{m,1}^0 + \partial_{x_2} u_{m,2}^1 \right) \qquad \text{in } \Omega_m^\varepsilon(t),$$

$$(3.8) \qquad \mathcal{O}(\varepsilon^2) = u_{m,2}^0 + \varepsilon u_{m,2}^1, \qquad \mathcal{O}(\varepsilon) = \partial_{x_2} u_{m,1}^0 \qquad \text{at } x_2 = 0,$$

$$(3.9) \qquad \mathcal{O}(\varepsilon) = \partial_{x_2} p_m^0 \qquad\qquad \text{at } x_2 = 0,$$

$$(3.10) \qquad \mathcal{O}(\varepsilon) = p_{\text{I}}^0 - p_{\text{in}}^0, \qquad \mathcal{O}(\varepsilon^2) = u_{\text{I},2}^0 + \varepsilon u_{\text{I},2}^1 \qquad \text{or}$$

$$(3.11) \qquad \mathcal{O}(\varepsilon^2) = \boldsymbol{u}_{\text{I}}^0 - \boldsymbol{u}_{\text{in}}^0 + \varepsilon \left(\boldsymbol{u}_{\text{I}}^1 - \boldsymbol{u}_{\text{in}}^1 \right) \qquad \text{at } x_1 = 0,$$

$$(3.12) \qquad \mathcal{O}(\varepsilon) = p_{\mathbb{II}}^0, \qquad \mathcal{O}(\varepsilon^2) = u_{\mathbb{II},2}^0 + \varepsilon u_{\mathbb{II},2}^1 \qquad \text{at } x_1 = 1,$$

$$(3.13) \qquad \mathcal{O}(\varepsilon) = u_{m,1}^0 + \lambda^0 \partial_{x_2} u_{m,1}^0 \qquad\qquad \text{at } x_2 = w^0(x_1),$$

$$(3.14) \qquad \mathcal{O}(\varepsilon^2) = u_{m,2}^0 + \varepsilon \left(u_{m,2}^1 + w^1 \partial_{x_2} u_{m,2}^0 - u_{m,1}^0 \partial_{x_1} w^0 \right) \qquad \text{at } x_2 = w^0(x_1).$$

Note that either (3.10) or (3.11) holds, depending on the choice of the boundary condition at the inlet $\Gamma_{\text{in}}^\varepsilon$.

Since we are interested in the flow behaviour away from the interface $\Gamma^\varepsilon(t)$, we define

$$G_{\text{I}}(t) := \min_{s \in [0,1]} \gamma_1^0(s,t), \qquad\qquad G_{\text{II}}(t) := \max_{s \in [0,1]} \gamma_1^0(s,t),$$

and investigate the problem for $x_1 < G_{\text{I}}(t)$ in fluid I and for $x_1 > G_{\text{II}}(t)$ in fluid II, respectively. In leading order, one obtains $\partial_{x_2} u_{m,2}^0 = 0$ in $\Omega_m^\varepsilon(t)$ for both $m \in \{\text{I}, \text{II}\}$ by the mass conservation (3.7). The symmetry and wall boundary conditions (3.8) and (3.14) lead to

$$u_{m,2}^0 = 0 \qquad\qquad \text{for } m = \text{I},\ x_1 < G_{\text{I}}(t),\ \text{and for } m = \text{II}, x_1 > G_{\text{II}}(t),$$

which agrees with the in- and outflow boundary conditions (3.10)–(3.12). The second component of the momentum balance of fluid I (3.4) yields in leading order $\partial_{x_2} p_{\text{I}}^0 = 0$ in $\Omega_{\text{I}}^\varepsilon(t)$, which is in agreement with the symmetry condition (3.9). We conclude

$$p_{\text{I}}^0 = p_{\text{I}}^0(t, x_1) \qquad\qquad \text{for } x_1 < G_{\text{I}}(t).$$

Analogously, the second component of the momentum balance of fluid II (3.6) leads to $\partial_{x_2} p_{\text{II}}^0 = 0$ in $\Omega_{\text{II}}^\varepsilon(t)$ (in agreement with the symmetry condition (3.9)), and thus

$$p_{\text{II}}^0 = p_{\text{II}}^0(t, x_1) \qquad\qquad \text{for } x_1 > G_{\text{II}}(t).$$

From the first component of the momentum balance of fluid I (3.3) one obtains

$$\partial_{x_1} p_{\text{I}}^0 = \partial_{x_2}^2 u_{\text{I},1}^0 \qquad\qquad \text{in } \Omega_{\text{I}}^\varepsilon(t).$$

Integrating twice over x_2 using the symmetry and wall boundary conditions (3.8) and (3.13), this leads to

$$(3.15) \qquad u_{\text{I},1}^0(t, \boldsymbol{x}) = \frac{x_2^2 - w^0(x_1)(2\lambda^0 + w^0(x_1))}{2} \partial_{x_1} p_{\text{I}}^0(t, x_1) \qquad \text{for } x_1 < G_{\text{I}}(t).$$

In a similar fashion, one obtains for fluid II by (3.5), (3.8), and (3.13)

$$(3.16) \qquad u_{\text{II},1}^0(t, \boldsymbol{x}) = \frac{x_2^2 - w^0(x_1)(2\lambda^0 + w^0(x_1))}{2M} \partial_{x_1} p_{\text{II}}^0(t, x_1) \qquad \text{for } x_1 > G_{\text{II}}(t).$$

Integrating (3.15) and (3.16) over $x_2 \in [0, w^0(x_1)]$ for any $x_1 < G_{\text{I}}$ and $x_1 > G_{\text{II}}$, respectively, and using Remark 2.2 yields

$$(3.17) \quad q(t) = \int_0^{w^0(a)} u_{\text{I},1}^0(t, \boldsymbol{x})|_{x_1 = a} dx_2 = -\frac{(w^0(x_1))^2(3\lambda^0 + w^0(x_1))}{3} \partial_{x_1} p_{\text{I}}^0(t, x_1),$$

$$(3.18) \quad q(t) = \int_0^{w^0(a)} u_{\text{II},1}^0(t, \boldsymbol{x})|_{x_1 = a} dx_2 = -\frac{(w^0(x_1))^2(3\lambda^0 + w^0(x_1))}{3M} \partial_{x_1} p_{\text{II}}^0(t, x_1),$$

where $q(t) := \int_0^1 u_{\text{I},1}^0(t, \boldsymbol{x}) dx_2$. Note that q is independent of x_1, and it is equivalent to the one in (A6) if (3.11) is given. Otherwise, q is unknown and must be found in

the further solution process. Solving the above equations for p^0_m, with the outflow boundary condition (3.12) we obtain

$$(3.19) \qquad p^0_{\mathrm{I}}(t, \boldsymbol{x}) = p^0_{\mathrm{in}}(t) - q(t) \int_0^{x_1} \frac{3}{(w^0(\xi))^2(3\lambda^0 + w^0(\xi))} d\xi \qquad \text{for } x_1 < G_{\mathrm{I}}(t),$$

$$(3.20) \qquad p^0_{\mathrm{II}}(t, \boldsymbol{x}) = q(t) \int_{x_1}^1 \frac{3M}{(w^0(\xi))^2(3\lambda^0 + w^0(\xi))} d\xi \qquad \text{for } x_1 > G_{\mathrm{II}}(t).$$

Here, the inlet pressure $p^0_{\mathrm{in}}(t)$ is either given by the inlet boundary condition (3.10), or has to be found in the further solution process. Note that since the inlet boundary condition is either (3.10) or (3.11), this means that either q or p^0_{in} is given, while the other still must be determined. Inserting (3.19) and (3.20) into (3.15) and (3.16) yields

$$(3.21) \qquad u^0_{\mathrm{I},1}(t, \boldsymbol{x}) = 3q(t) \frac{w^0(x_1)(2\lambda^0 + w^0(x_1)) - x_2^2}{2(w^0(x_1))^2(3\lambda^0 + w^0(x_1))} \qquad \text{for } x_1 < G_{\mathrm{I}}(t),$$

$$(3.22) \qquad u^0_{\mathrm{II},1}(t, \boldsymbol{x}) = 3q(t) \frac{w^0(x_1)(2\lambda^0 + w^0(x_1)) - x_2^2}{2(w^0(x_1))^2(3\lambda^0 + w^0(x_1))} \qquad \text{for } x_1 > G_{\mathrm{II}}(t).$$

Using (3.21) and (3.22) in the mass conservation (3.7), the first order equations become

$$\partial_{x_2} u^1_{m,2} = q(t) \left(\frac{1}{2(3\lambda^0 + w^0(x_1))^2} + \frac{1}{(w^0(x_1))^2} \right.$$
$$\left. - \frac{9(2\lambda^0 + w^0(x_1))x_2^2}{2(w^0(x_1))^3(3\lambda^0 + w^0(x_1))^2} \right) \partial_{x_1} w^0(x_1),$$

for $m \in \{\mathrm{I}, \mathrm{II}\}$. Integration over x_2 using the symmetry condition (3.8) yields

$$u^1_{\mathrm{I},2}(t, \boldsymbol{x}) = q(t) \left(\frac{x_2}{2(3\lambda^0 + w^0(x_1))^2} + \frac{x_2}{(w^0(x_1))^2} \right.$$
$$\left. - \frac{3(2\lambda^0 + w^0(x_1))x_2^3}{2(w^0(x_1))^3(3\lambda^0 + w^0(x_1))^2} \right) \partial_{x_1} w^0(x_1) \quad \text{for } x_1 < G_{\mathrm{I}}(t),$$

$$u^1_{\mathrm{II},2}(t, \boldsymbol{x}) = q(t) \left(\frac{x_2}{2(3\lambda^0 + w^0(x_1))^2} + \frac{x_2}{(w^0(x_1))^2} \right.$$
$$\left. - \frac{3(2\lambda^0 + w^0(x_1))x_2^3}{2(w^0(x_1))^3(3\lambda^0 + w^0(x_1))^2} \right) \partial_{x_1} w^0(x_1) \quad \text{for } x_1 > G_{\mathrm{II}}(t),$$

which is in agreement with the boundary conditions (3.10)–(3.12) and (3.14).

Summarizing, we obtain the following solution in the bulk domains. There holds

$$\boldsymbol{u}^\varepsilon_{\mathrm{I}}(t, \boldsymbol{x}) = q(t) \cdot$$

$$(3.23) \qquad \begin{pmatrix} 3\frac{w^0(x_1)(2\lambda^0 + w^0(x_1)) - x_2^2}{2(w^0(x_1))^2(3\lambda^0 + w^0(x_1))} + \mathcal{O}(\varepsilon) \\ \varepsilon \left(\frac{x_2}{2(3\lambda^0 + w^0(x_1))^2} + \frac{x_2}{(w^0(x_1))^2} - \frac{3(2\lambda^0 + w^0(x_1))x_2^3}{2(w^0(x_1))^3(3\lambda^0 + w^0(x_1))^2} \right) \partial_{x_1} w^0(x_1) + \mathcal{O}(\varepsilon^2) \end{pmatrix},$$

$$(3.24) \quad p^\varepsilon_{\mathrm{I}}(t, \boldsymbol{x}) = p^0_{\mathrm{in}}(t) - q(t) \int_0^{x_1} \frac{3}{(w^0(\xi))^2(3\lambda^0 + w^0(\xi))} d\xi + \mathcal{O}(\varepsilon),$$

for $x_1 < G_{\mathrm{I}}(t)$, while for $x_1 > G_{\mathrm{II}}(t)$ one gets

$$\boldsymbol{u}_{\mathrm{II}}^{\varepsilon}(t, \boldsymbol{x}) = q(t) \cdot$$

$$(3.25) \quad \begin{pmatrix} 3\frac{w^0(x_1)(2\lambda^0 + w^0(x_1)) - x_2^2}{2(w^0(x_1))^2(3\lambda^0 + w^0(x_1))} + \mathcal{O}(\varepsilon) \\ \varepsilon\left(\frac{x_2}{2(3\lambda^0 + w^0(x_1))^2} + \frac{x_2}{(w^0(x_1))^2} - \frac{3(2\lambda^0 + w^0(x_1))x_2^3}{2(w^0(x_1))^3(3\lambda^0 + w^0(x_1))^2}\right)\partial_{x_1} w^0(x_1) + \mathcal{O}(\varepsilon^2) \end{pmatrix},$$

$$(3.26) \quad p_{\mathrm{II}}^{\varepsilon}(t, \boldsymbol{x}) = q(t) \int_{x_1}^{1} \frac{3\mathrm{M}}{(w^0(\xi))^2(3\lambda^0 + w^0(\xi))} d\xi + \mathcal{O}(\varepsilon).$$

This means that the solution in the bulk domains is of Hagen-Poiseuille type. Depending on the chosen inlet boundary condition (3.10) or (3.11), either the inlet pressure p_{in}^0 or the total flux q is given. The other coefficient will be determined in the following subsection via the coupling at the interface $\Gamma^{\varepsilon}(t)$. For upscaled models, we emphasize that the total flux q is independent of the position x_1 and that the pressures p_m^0, $m \in \{\mathrm{I}, \mathrm{II}\}$, depend linearly on q with a coefficient that only depends on the geometry (w^0), the viscosity ratio M and the slip length λ^0.

3.2. Interface with small deformations. We continue the analysis for the interface region around $\Gamma^{\varepsilon}(t)$. We first show that the bulk solutions are not compatible with the interface conditions (2.23)–(2.26). However, introduction of a suitable scaling allows to find the asymptotic solution in the boundary layer around the interface $\Gamma^{\varepsilon}(t)$, which connects the bulk domain solutions. Additionally to (A1)–(A6), we make the following assumptions.

(A7) The leading order interface position in x_1 is constant, i.e., $\partial_s \gamma_1^0 \equiv 0$.

(A8) The capillary number is given by $\mathrm{Ca} = \varepsilon^{\alpha}\overline{\mathrm{Ca}}$ for some $\alpha \in \mathbb{N}_0$. Here, $\overline{\mathrm{Ca}}$ denotes the effective capillary number and is independent of ε.

Note that (A7) means that the fluid-fluid interface Γ^{ε} has only small deformations, such that $G_{\mathrm{I}}(t) = \gamma_1^0(t) = G_{\mathrm{II}}(t)$. Furthermore, (A8) is used to distinguish whether interfacial tension is relevant or even dominating the interface movement, see also Remark 3.1. In case of a largely deformed interface ($\partial_s \gamma_1^0 \neq 0$), the solution could violate the boundary and symmetry conditions (2.25) and (2.26). A more detailed analysis with further boundary layers would be necessary, but lies out of the scope of this paper.

Inserting the homogenization ansatz into the kinematic interface condition (2.23) gives

$$(\partial_t \gamma_1^0 - u_{\mathrm{I},1}^0)\partial_s \gamma_2^0 + u_{\mathrm{I},2}^0 \partial_s \gamma_1^1 = \mathcal{O}(\varepsilon).$$

Since γ_1^0 is constant in the parameter s, a non-singular parameterization requires $\partial_s \gamma_2^0 > 0$. Inserting the bulk solution (3.23), where $u_{\mathrm{I},2}^0 = 0$, yields in leading order

$$\partial_t \gamma_1^0 = 3q\frac{w^0(\gamma_1^0)(2\lambda^0 + w^0(\gamma_1^0)) - (\gamma_2^0)^2}{2(w^0(\gamma_1^0))^2(3\lambda^0 + w^0(\gamma_1^0))},$$

which contradicts the assumption that γ_1^0 does not depend on s, except for the trivial case $q(t) = 0$. Therefore, we expect the existence of a boundary layer around the interface $\Gamma^{\varepsilon}(t)$.

To resolve the boundary layer, we apply the inner scaling

$$X_1(t, x_1) := (x_1 - \gamma_1^0(t))/\varepsilon, \qquad\qquad X_2 := x_2$$

and use the rescaled variables and domains

$$\boldsymbol{Y}^\varepsilon := \begin{pmatrix} (\gamma_1^\varepsilon - \gamma_1^0)/\varepsilon \\ \gamma_2^\varepsilon \end{pmatrix}, \quad \boldsymbol{U}_m^\varepsilon(t, \boldsymbol{X}) := \boldsymbol{u}_m^\varepsilon(t, \boldsymbol{x}), \quad P_m^\varepsilon(t, \boldsymbol{X}) := p_m^\varepsilon(t, \boldsymbol{x}),$$

$$\Omega_{\boldsymbol{x}}^\varepsilon(t) := \{\boldsymbol{X} \in \mathbb{R}^2 \mid 0 < X_2 < w^\varepsilon(\gamma_1^0(t) + \varepsilon X_1)\}, \quad \Gamma_{\boldsymbol{x}}^\varepsilon(t) := \{\boldsymbol{Y}^\varepsilon(t, s) \mid s \in [0,1]\},$$

$$\Omega_{\boldsymbol{x},\mathrm{I}}^\varepsilon(t) := \{\boldsymbol{X}(t, \boldsymbol{x}) \mid \boldsymbol{x} \in \Omega_{\mathrm{I}}^\varepsilon\}, \quad \Omega_{\boldsymbol{x},\mathrm{II}}^\varepsilon(t) := \{\boldsymbol{X}(t, \boldsymbol{x}) \mid \boldsymbol{x} \in \Omega_{\mathrm{II}}^\varepsilon\},$$

$$\Gamma_{\boldsymbol{x},\mathrm{w},m}^\varepsilon(t) := \{\boldsymbol{X} \in \partial\Omega_{\boldsymbol{x},m}^\varepsilon(t) \mid X_2 = w^\varepsilon(\gamma_1^0(t) + \varepsilon X_1)\}.$$

The matching conditions between inner expansion in terms of $\boldsymbol{X}$ and outer expansion in terms of $\boldsymbol{x}$ require the equivalence in the limit, i.e., for any quantity $a_m^\varepsilon(t, \boldsymbol{x})$ with inner expansion $A_m^\varepsilon(t, \boldsymbol{X})$ there must hold $\lim_{x_1 \to \gamma_1^0} a_m^\varepsilon(t, \boldsymbol{x}) = \lim_{X_1 \to (-1)^m \infty} A_m^\varepsilon(t, \boldsymbol{X})|_{X_2=x_2}$. With the rescaled coordinates, (2.15)–(2.19) and (2.22)–(2.26) become

(3.27)
$$\varepsilon^2 \mathrm{Re}\big(\varepsilon\partial_t \boldsymbol{U}_\mathrm{I}^\varepsilon - \partial_{X_1}\boldsymbol{U}_\mathrm{I}^\varepsilon \partial_t \gamma_1^0 + (\boldsymbol{U}_\mathrm{I}^\varepsilon \cdot \nabla_{\boldsymbol{x}})\boldsymbol{U}_\mathrm{I}^\varepsilon\big) + \nabla_{\boldsymbol{x}} P_\mathrm{I}^\varepsilon = \varepsilon\,\Delta_{\boldsymbol{x}}\boldsymbol{U}_\mathrm{I}^\varepsilon \qquad \text{in } \Omega_{\boldsymbol{x},\mathrm{I}}^\varepsilon(t),$$

(3.28)
$$\varepsilon^2 \mathrm{RRe}\big(\varepsilon\partial_t \boldsymbol{U}_\mathrm{II}^\varepsilon - \partial_{X_1}\boldsymbol{U}_\mathrm{II}^\varepsilon \partial_t \gamma_1^0 + (\boldsymbol{U}_\mathrm{II}^\varepsilon \cdot \nabla_{\boldsymbol{x}})\boldsymbol{U}_\mathrm{II}^\varepsilon\big) + \nabla_{\boldsymbol{x}} P_\mathrm{II}^\varepsilon = \mathrm{M}\varepsilon\,\Delta_{\boldsymbol{x}}\boldsymbol{U}_\mathrm{II}^\varepsilon \quad \text{in } \Omega_{\boldsymbol{x},\mathrm{II}}^\varepsilon(t),$$

$$
\begin{aligned}
(3.29) && \nabla_{\boldsymbol{x}}\cdot \boldsymbol{U}_m^\varepsilon &= 0 && \text{in } \Omega_{\boldsymbol{x},m}^\varepsilon(t), \\
(3.30) && \boldsymbol{U}_m^\varepsilon \cdot \boldsymbol{n}_\mathrm{sym} = 0, \quad \boldsymbol{t}_\mathrm{sym} \cdot \nabla_{\boldsymbol{x}}\boldsymbol{U}_m^\varepsilon \boldsymbol{n}_\mathrm{sym} &= 0 && \text{at } X_2 = 0, \\
(3.31) && \nabla_{\boldsymbol{x}} P_m^\varepsilon \cdot \boldsymbol{n}_\mathrm{sym} &= 0, && \text{at } X_2 = 0, \\
(3.32) && \boldsymbol{T}_\mathrm{w}^\varepsilon \cdot \big(\boldsymbol{U}_m^\varepsilon + 2\lambda^\varepsilon\,\mathbf{D}_{\boldsymbol{x}}(\boldsymbol{U}_m^\varepsilon)\boldsymbol{N}_\mathrm{w}^\varepsilon\big) = 0, \quad \boldsymbol{U}_m^\varepsilon \cdot \boldsymbol{N}_\mathrm{w}^\varepsilon &= 0 && \text{on } \Gamma_{\boldsymbol{x},\mathrm{w},m}^\varepsilon(t), \\
(3.33) && \partial_t \gamma_1^0 N_{\Gamma,1}^\varepsilon + \varepsilon\partial_t \boldsymbol{Y}^\varepsilon \cdot \boldsymbol{N}_\Gamma^\varepsilon = \boldsymbol{U}_\mathrm{I}^\varepsilon \cdot \boldsymbol{N}_\Gamma^\varepsilon, \quad \boldsymbol{U}_\mathrm{I}^\varepsilon &= \boldsymbol{U}_\mathrm{II}^\varepsilon && \text{on } \Gamma_{\boldsymbol{x}}^\varepsilon(t), \\
(3.34) && -(P_\mathrm{I}^\varepsilon - P_\mathrm{II}^\varepsilon)\boldsymbol{N}_\Gamma^\varepsilon + 2\varepsilon\big(\mathbf{D}_{\boldsymbol{x}}(\boldsymbol{U}_\mathrm{I}^\varepsilon) - \mathrm{M}\,\mathbf{D}_{\boldsymbol{x}}(\boldsymbol{U}_\mathrm{II}^\varepsilon)\big)\boldsymbol{N}_\Gamma^\varepsilon = \tfrac{\varepsilon^2}{\mathrm{Ca}}K^\varepsilon \boldsymbol{N}_\Gamma^\varepsilon && \text{on } \Gamma_{\boldsymbol{x}}^\varepsilon(t), \\
(3.35) && \boldsymbol{N}_\Gamma^\varepsilon \cdot \boldsymbol{n}_\mathrm{sym} &= 0 && \text{at } s = 0, \\
(3.36) && \cos(\theta^\varepsilon(-\partial_t(\gamma_1^0 T_{\mathrm{w},1}^\varepsilon + \varepsilon\boldsymbol{Y}^\varepsilon \cdot \boldsymbol{T}_\mathrm{w}^\varepsilon)|_{X_1=Y_1^\varepsilon})) = \boldsymbol{T}_\Gamma^\varepsilon \cdot \boldsymbol{T}_\mathrm{w}^\varepsilon\big|_{X_1=Y_1^\varepsilon} && \text{at } s = 1.
\end{aligned}
$$

The transformed normal and tangential vectors are given by

$$\boldsymbol{T}_\mathrm{w}^\varepsilon = \boldsymbol{t}_\mathrm{w}^\varepsilon\big|_{x_1=\gamma_1^0+\varepsilon X_1}, \qquad\qquad \boldsymbol{N}_\mathrm{w}^\varepsilon = \boldsymbol{n}_\mathrm{w}^\varepsilon\big|_{x_1=\gamma_1^0+\varepsilon X_1},$$

$$\boldsymbol{T}_\Gamma^\varepsilon = \frac{1}{\sqrt{(\partial_s Y_1^\varepsilon)^2 + (\partial_s Y_2^\varepsilon)^2}}\partial_s \boldsymbol{Y}^\varepsilon, \qquad \boldsymbol{N}_\Gamma^\varepsilon = \frac{1}{\sqrt{(\partial_s Y_1^\varepsilon)^2 + (\partial_s Y_2^\varepsilon)^2}}\begin{pmatrix} \partial_s Y_2^\varepsilon \\ -\partial_s Y_1^\varepsilon \end{pmatrix},$$

and the rescaled curvature K^ε is

$$K^\varepsilon = \frac{\partial_s Y_1^\varepsilon \partial_s^2 Y_2^\varepsilon - \partial_s Y_2^\varepsilon \partial_s^2 Y_1^\varepsilon}{\varepsilon\big((\partial_s Y_1^\varepsilon)^2 + (\partial_s Y_2^\varepsilon)^2\big)^{3/2}}.$$

Inserting the homogenization ansatz into (3.27)–(3.36) using (A1)–(A5), (A7),

(A8) and a Taylor expansion around $X_2 = w^0(\gamma_1^0(t))$ for (3.32), one obtains

$$(3.37) \qquad \mathcal{O}(\varepsilon^2) = \nabla_{\boldsymbol{x}} P_{\mathrm{I}}^0 + \varepsilon \left(\nabla_{\boldsymbol{x}} P_{\mathrm{I}}^1 - \Delta_{\boldsymbol{x}} \boldsymbol{U}_{\mathrm{I}}^0 \right) \qquad \text{in } \Omega_{\boldsymbol{x},\mathrm{I}}^\varepsilon(t),$$

$$(3.38) \qquad \mathcal{O}(\varepsilon^2) = \nabla_{\boldsymbol{x}} P_{\mathrm{II}}^0 + \varepsilon \left(\nabla_{\boldsymbol{x}} P_{\mathrm{II}}^1 - \mathrm{M}\,\Delta_{\boldsymbol{x}} \boldsymbol{U}_{\mathrm{II}}^0 \right) \qquad \text{in } \Omega_{\boldsymbol{x},\mathrm{II}}^\varepsilon(t),$$

$$(3.39) \qquad \mathcal{O}(\varepsilon) = \nabla_{\boldsymbol{x}} \cdot \boldsymbol{U}_m^0 \qquad \text{in } \Omega_{\boldsymbol{x},m}^\varepsilon(t),$$

$$(3.40) \qquad \mathcal{O}(\varepsilon) = U_{m,2}^0, \qquad \mathcal{O}(\varepsilon) = \partial_{X_2} U_{m,1}^0 \qquad \text{at } X_2 = 0,$$

$$(3.41) \qquad \mathcal{O}(\varepsilon^2) = \partial_{X_2} P_m^0 + \varepsilon \partial_{X_2} P_m^1 \qquad \text{at } X_2 = 0,$$

$$(3.42) \qquad \mathcal{O}(\varepsilon) = U_{m,1}^0 + \left(\lambda^0 + \lambda_e \exp(-|X_1|) \right)$$
$$\cdot \left(\partial_{X_2} U_{m,1}^0 + \partial_{X_1} U_{m,2}^0 \right) \qquad \text{at } X_2 = w^0(\gamma_1^0(t)),$$

$$(3.43) \qquad \mathcal{O}(\varepsilon) = U_{m,2}^0 \qquad \text{at } X_2 = w^0(\gamma_1^0(t)),$$

$$(3.44) \qquad \mathcal{O}(\varepsilon) = \left(\partial_t \gamma_1^0 - U_{\mathrm{I},1}^0 \right) \partial_s Y_2^0 + U_{\mathrm{I},2}^0 \partial_s Y_1^0 \qquad \text{on } \Gamma_{\boldsymbol{x}}^\varepsilon(t),$$

$$(3.45) \qquad \mathcal{O}(\varepsilon) = \boldsymbol{U}_{\mathrm{I}}^0 - \boldsymbol{U}_{\mathrm{II}}^0 \qquad \text{on } \Gamma_{\boldsymbol{x}}^\varepsilon(t),$$

$$(3.46)$$
$$\mathcal{O}(\varepsilon^{\min(1,2-\alpha)}) = \left(P_{\mathrm{I}}^0 - P_{\mathrm{II}}^0 \right) + \frac{\varepsilon^{1-\alpha}}{\overline{\mathrm{Ca}}} \frac{\partial_s Y_1^0 \partial_s^2 Y_2^0 - \partial_s Y_2^0 \partial_s^2 Y_1^0}{\left((\partial_s Y_1^0)^2 + (\partial_s Y_2^0)^2 \right)^{3/2}} \qquad \text{on } \Gamma_{\boldsymbol{x}}^\varepsilon(t),$$

$$(3.47) \qquad \mathcal{O}(\varepsilon) = \partial_s \boldsymbol{Y}^0 \cdot \left(\mathbf{D}_{\boldsymbol{x}}(\boldsymbol{U}_{\mathrm{I}}^0) - \mathrm{M}\,\mathbf{D}_{\boldsymbol{x}}(\boldsymbol{U}_{\mathrm{II}}^0) \right) \begin{pmatrix} \partial_s Y_2^0 \\ -\partial_s Y_1^0 \end{pmatrix} \qquad \text{on } \Gamma_{\boldsymbol{x}}^\varepsilon(t),$$

$$(3.48) \qquad \mathcal{O}(\varepsilon) = \partial_s Y_1^0 \qquad \text{at } s = 0,$$

$$(3.49) \qquad \mathcal{O}(\varepsilon) = \frac{\partial_s Y_1^0}{\sqrt{(\partial_s Y_1^0)^2 + (\partial_s Y_2^0)^2}} + \cos(\theta^0(\partial_t \gamma_1^0)) \qquad \text{at } s = 1.$$

The leading order terms in the momentum equations (3.37) and (3.38) yield $\nabla_{\boldsymbol{x}} P_m^0 = \mathbf{0}$ in $\Omega_{\boldsymbol{x},m}^\varepsilon(t)$ for $m \in \{\mathrm{I}, \mathrm{II}\}$. This is in agreement with the symmetry condition (3.41). By matching with the outer solution we obtain

$$(3.50) \qquad P_m^0(t, \boldsymbol{X}) = p_m^0(t, \gamma_1^0(t)) \qquad \text{for all } \boldsymbol{X} \in \Omega_{\boldsymbol{x},m}^\varepsilon(t).$$

Remark 3.1. Recall that we assume $\mathrm{Ca} = \varepsilon^\alpha \overline{\mathrm{Ca}}$ for some $\alpha \in \mathbb{N}_0$. Considering (3.46), one must distinguish the cases $\alpha < 1$, $\alpha = 1$ and $\alpha > 1$. For $\alpha < 1$, the interface tension force is negligible in leading order, such that the pressures P_{I}^0 and P_{II}^0 are equal. Formally, this allows to determine the leading order solution of the outer bulk-flow problem. However, this also means that the interface $\Gamma_{\boldsymbol{x}}^\varepsilon(t)$ is not stabilized by surface tension, but part of the first order solution, such that we cannot guarantee solvability. Furthermore, one might expect the occurrence of topological changes due to e.g. formation of bubbles, thin films, etc. which are not part of this model. In the case $\alpha > 1$, the interfacial tension force is dominating (3.46), so that the leading order curvature K^0 of the interface is zero. Due to the boundary conditions (3.48) and (3.49), this can only happen if the leading order contact angle $\theta^0(\partial_t \gamma_1^0)$ is $\pi/2$ for any $\gamma_1^0(t)$, i.e., for a constant contact angle model for perfectly mixed-wet materials. Even worse, due to (3.50), the leading order solution of the outer bulk-flow problem then depends on the first order solution, such that we cannot assure the solvability in this case either. We therefore consider in what follows only the case $\alpha = 1$. Then the pressure difference is balanced by the surface tension force in (3.46). This leads to a solution for the outer bulk-flow problem as well as for the interface shape.

In the regime $\alpha = 1$, plugging the constant pressures (3.50) into the interfacial

force balance (3.46) yields a constant leading-order curvature K^0 given by

$$(3.51) \qquad K^0 = \frac{\partial_s Y_2^0 \partial_s^2 Y_1^0 - \partial_s Y_1^0 \partial_s^2 Y_2^0}{((\partial_s Y_1^0)^2 + (\partial_s Y_2^0)^2)^{3/2}} = \overline{\mathrm{Ca}}(p_{\mathrm{I\!I}}^0 - p_{\mathrm{I}}^0)|_{x_1 = \gamma_1^0}.$$

Therefore, the interface is a circular arc. By the contact-angle condition (3.49), one obtains

$$(3.52) \qquad K^0 = -\frac{\cos(\theta^0(\partial_t \gamma_1^0))}{w^0(\gamma_1^0)}.$$

Combining (3.51) and (3.52) and plugging in the bulk pressure solutions (3.24) and (3.26) leads to

$$(3.53) \qquad p_{\mathrm{in}}^0 - q \left(\int_0^{\gamma_1^0} \frac{3}{(w^0(x_1))^2(3\lambda^0 + w^0(x_1))} dx_1 + \int_{\gamma_1^0}^1 \frac{3M}{(w^0(x_1))^2(3\lambda^0 + w^0(x_1))} dx_1 \right)$$
$$= \frac{\cos(\theta^0(\partial_t \gamma_1^0))}{\overline{\mathrm{Ca}} w^0(\gamma_1^0)}.$$

Due to the constant curvature (3.52) and the symmetry condition (3.48), the leading order interface $\Gamma_{\boldsymbol{X}}^0(t) := \{\boldsymbol{Y}^0(t,s) \mid s \in [0,1]\}$ is given (up to a reparametrization) by

$$\boldsymbol{Y}^0(t,s) = \begin{cases} \frac{w^0(\gamma_1^0)}{\cos(\theta^0(\partial_t \gamma_1^0))} \begin{pmatrix} \cos\left((\frac{\pi}{2} - \theta^0(\partial_t \gamma_1^0))s\right) - \sin\left(\theta^0(\partial_t \gamma_1^0)\right) \\ \sin\left((\frac{\pi}{2} - \theta^0(\partial_t \gamma_1^0))s\right) \end{pmatrix} & \text{for } \theta^0 \neq \pi/2, \\ w^0(\gamma_1^0(t))\begin{pmatrix} 0 \\ s \end{pmatrix} & \text{for } \theta^0 = \pi/2. \end{cases}$$

Analogously to Remark 2.2, by the mass conservation (2.17), the interface velocity (3.33) and the outer velocity solution (3.23), we obtain

$$0 = \int_{\Omega_{\mathrm{I}}^\varepsilon} \nabla^\varepsilon \cdot \boldsymbol{u}_{\mathrm{I}}^\varepsilon d\boldsymbol{x} = \int_{\Gamma^\varepsilon} \boldsymbol{u}_{\mathrm{I}}^\varepsilon \cdot \boldsymbol{n}_{\Gamma}^\varepsilon dl - \int_0^1 u_{\mathrm{I},1}^\varepsilon \big|_{x_1=0} dx_1$$
$$= \int_{\Gamma^\varepsilon} \partial_t \gamma_1^0 N_{\Gamma,1}^\varepsilon + \varepsilon \partial_t \boldsymbol{Y}^\varepsilon \cdot \boldsymbol{N}_{\Gamma}^\varepsilon dl - q + \mathcal{O}(\varepsilon) = \int_0^1 \partial_t \gamma_1^0 \partial_s Y_2^\varepsilon ds - q + \mathcal{O}(\varepsilon)$$
$$= \partial_t \gamma_1^0 w^0(\gamma_1^0) - q + \mathcal{O}(\varepsilon).$$

Therefore, the leading order position γ_1^0 of the interface fulfils

$$(3.54) \qquad \partial_t \gamma_1^0(t) = \frac{q(t)}{w^0(\gamma_1^0(t))}.$$

To find the solution for $\boldsymbol{u}_m^0, p_m^0$ ($m \in \{\mathrm{I}, \mathrm{I\!I}\}$), which is given by (3.23)–(3.26), one has to determine γ_1^0, q and p_{in}^0. The derivation depends on the chosen inlet boundary condition. For a given inlet velocity $\boldsymbol{u}_{\mathrm{I}}^\varepsilon = \boldsymbol{u}_{\mathrm{in}}^\varepsilon$ at $\Gamma_{\mathrm{in}}^\varepsilon$, the value of q is known. Plugging q into (3.54) and solving for γ_1^0 yields

$$\gamma_1^0(t) = \mathcal{W}^{-1} \left(\mathcal{W}(\gamma_1^0|_{t=0}) + \int_0^t q(\tau) d\tau \right),$$

where $\mathcal{W}(\xi) := \int_0^\xi w^0(x_1) dx_1$. Note that $\mathcal{W}' = w^0 > 0$ by (A4), such that the inverse function $\mathcal{W}^{-1}$ is well-defined. Finally, p_{in}^0 can be found by (3.53).

For a given inlet pressure $p_{\mathrm{I}}^{\varepsilon} = p_{\mathrm{in}}^{\varepsilon}$ at $\Gamma_{\mathrm{in}}^{\varepsilon}$, the value of p_{in}^0 is known. Then, the differential algebraic system (3.53) and (3.54) has index 1 and can be solved for q and γ_1^0. A sufficient condition for solvability is

$$\sin\left(\theta^0\left(\tfrac{q}{w^0(\gamma_1^0)}\right)\right)(\theta^0)'\left(\tfrac{q}{w^0(\gamma_1^0)}\right)$$

$$\neq \overline{\mathrm{Ca}}(w^0(\gamma_1^0))^2\left(\int_0^{\gamma_1^0} \frac{3}{(w^0(x_1))^2(3\lambda^0+w^0(x_1))}dx_1 + \int_{\gamma_1^0}^1 \frac{3\mathrm{M}}{(w^0(x_1))^2(3\lambda^0+w^0(x_1))}dx_1\right),$$

where $(\theta^0)'$ denotes the derivative of θ^0. Note that the righthand side is always positive, so that any contact angle model which fulfils $(\theta^0)' \leq 0$ yields solvable differential algebraic equations.

Furthermore, from (3.37)–(3.45) and (3.47), the velocity close to the interface is given by two coupled Stokes problems. More precisely, these problems are defined in the domains

$$\Omega_{\mathbf{x},\mathrm{I}}^0(t) = \{\mathbf{X} \in \mathbb{R} \times (0, w^0(\gamma_1^0(t))) \mid \exists s \in [0,1]: X_1 < Y_1^0(t,s) \wedge X_2 = Y_2^0(t,s)\},$$
$$\Omega_{\mathbf{x},\mathbb{II}}^0(t) = \{\mathbf{X} \in \mathbb{R} \times (0, w^0(\gamma_1^0(t))) \mid \exists s \in [0,1]: X_1 > Y_1^0(t,s) \wedge X_2 = Y_2^0(t,s)\}.$$

With this, the two problems are $(m \in \{\mathrm{I}, \mathbb{II}\})$

$$(3.55)\quad 0 = \nabla_{\mathbf{x}}P_{\mathrm{I}}^1 - \Delta_{\mathbf{x}}\mathbf{U}_{\mathrm{I}}^0 \qquad\qquad\qquad\qquad \text{in } \Omega_{\mathbf{x},\mathrm{I}}^0(t),$$

$$(3.56)\quad 0 = \nabla_{\mathbf{x}}P_{\mathbb{II}}^1 - \mathrm{M}\,\Delta_{\mathbf{x}}\mathbf{U}_{\mathbb{II}}^0 \qquad\qquad\qquad \text{in } \Omega_{\mathbf{x},\mathbb{II}}^0(t),$$

$$(3.57)\quad 0 = \nabla_{\mathbf{x}}\cdot\mathbf{U}_m^0 \qquad\qquad\qquad\qquad\qquad\quad \text{in } \Omega_{\mathbf{x},m}^0(t),$$

$$(3.58)\quad 0 = U_{m,2}^0, \qquad 0 = \partial_{X_2}U_{m,1}^0, \qquad 0 = \partial_{X_2}P_m^1 \qquad \text{at } X_2 = 0,$$

$$(3.59)\quad 0 = U_{m,1}^0 + \left(\lambda^0 + \lambda_e\exp(-|X_1|)\right)\partial_{X_2}U_{m,1}^0, \quad 0 = U_{m,2}^0 \quad \text{at } X_2 = w^0(\gamma_1^0(t)),$$

$$(3.60)\quad 0 = \left(\partial_t\gamma_1^0 - U_{\mathrm{I},1}^0\right)\partial_s Y_2^0 + U_{\mathrm{I},2}^0\partial_s Y_1^0 \qquad\qquad \text{on } \Gamma_{\mathbf{x}}^0(t),$$

$$(3.61)\quad 0 = \mathbf{U}_{\mathrm{I}}^0 - \mathbf{U}_{\mathbb{II}}^0 \qquad\qquad\qquad\qquad\qquad\quad \text{on } \Gamma_{\mathbf{x}}^0(t),$$

$$(3.62)\quad 0 = \partial_s\mathbf{Y}^0 \cdot \left(\mathbf{D}_{\mathbf{x}}(\mathbf{U}_{\mathrm{I}}^0) - \mathrm{M}\,\mathbf{D}_{\mathbf{x}}(\mathbf{U}_{\mathbb{II}}^0)\right)\begin{pmatrix} \partial_s Y_2^0 \\ -\partial_s Y_1^0 \end{pmatrix} \qquad \text{on } \Gamma_{\mathbf{x}}^0(t),$$

$$(3.63)\quad \mathbf{0} = \lim_{X_1\to-\infty}\mathbf{U}_{\mathrm{I}}^0 - \mathbf{u}_{\mathrm{I}}^0|_{x_1=\gamma_1^0, x_2=X_2},$$

$$(3.64)\quad \mathbf{0} = \lim_{X_1\to\infty}\mathbf{U}_{\mathbb{II}}^0 - \mathbf{u}_{\mathbb{II}}^0|_{x_1=\gamma_1^0, x_2=X_2}.$$

3.3. Unsaturated flow limit. In (A2) we assumed the viscosity ratio $\mathrm{M} = \mathcal{O}(\varepsilon^0)$. Here, we investigate the case when the viscosity of fluid $\mathbb{II}$ is much smaller than that of fluid I, like in a system consisting of water and air. Hence, we replace (A2) by:

(A9) The viscosity ratio satisfies $M = \mathcal{O}(\varepsilon^\beta)$ for some $\beta \geq 1$.

Following the same steps as in the previous subsections, we obtain a model which only includes the flow of fluid I, while the flow of fluid $\mathbb{II}$ can be omitted. In other words, the upscaled model is an unsaturated flow in the thin strip. Furthermore, the effective solution for fluid I will coincide with the one obtained when letting $M \to 0$ in (3.23), (3.24), (3.53), and (3.54) derived previously.

To this end, we use the same asymptotic expansions and (A1), (A3)–(A8) and (A9) instead of (A2). For fluid I, we obtain again (3.3), (3.4), (3.7)–(3.9), (3.13), and (3.14) and work with either (3.10) or (3.11) as inlet condition. Therefore, the solution for fluid I is again (3.23) and (3.24), where p_{in}^0 and q are given by the interface region and the inlet condition.

For fluid $\mathbb{II}$, the leading order mass balance equations become

$$(3.65) \qquad \mathcal{O}(\varepsilon) = \partial_{x_1} p^0_{\mathbb{II}} \qquad\qquad\qquad \text{in } \Omega^\varepsilon_{\mathbb{II}}(t),$$

$$(3.66) \qquad \mathcal{O}(\varepsilon^0) = \varepsilon^{-1} \partial_{x_2} p^0_{\mathbb{II}} \qquad\qquad \text{in } \Omega^\varepsilon_{\mathbb{II}}(t).$$

Together with the leading order outflow condition $\mathcal{O}(\varepsilon) = p^0_{\mathbb{II}}$ at $x_1 = 1$, we conclude that $p^0_{\mathbb{II}}(t, \boldsymbol{x}) = 0$ in $\Omega^\varepsilon_{\mathbb{II}}(t)$. Rescaling the interface region as in subsection 3.2 and taking (A7) and (A8) into account, the leading order equations for fluid I are again (3.37) and (3.39)–(3.43). Since $p^0_{\mathbb{II}} \equiv 0$, the interface conditions are (3.42)–(3.44) and (3.48), as well as

$$(3.67) \qquad \mathcal{O}(\varepsilon^{\min(1,2-\alpha)}) = P^0_{\mathrm{I}} + \frac{\varepsilon^{1-\alpha}}{\overline{\mathrm{Ca}}} \frac{\partial_s Y^0_1 \partial^2_s Y^0_2 - \partial_s Y^0_2 \partial^2_s Y^0_1}{\left((\partial_s Y^0_1)^2 + (\partial_s Y^0_2)^2\right)^{3/2}} \qquad \text{on } \Gamma^\varepsilon_{\boldsymbol{x}}(t),$$

$$(3.68) \qquad \mathcal{O}(\varepsilon) = \partial_s \boldsymbol{Y}^0 \cdot \mathbf{D}_{\boldsymbol{x}}(\boldsymbol{U}^0_{\mathrm{I}}) \begin{pmatrix} \partial_s Y^0_2 \\ -\partial_s Y^0_1 \end{pmatrix} \qquad \text{on } \Gamma^\varepsilon_{\boldsymbol{x}}(t).$$

In the regime $\alpha = 1$, this yields a constant leading-order curvature, implying

$$(3.69) \qquad p^0_{\mathrm{in}} - q \int_0^{\gamma^0_1} \frac{3}{(w^0(x_1))^2(3\lambda^0 + w^0(x_1))} dx_1 = \frac{\cos(\theta^0(\partial_t \gamma^0_1))}{\overline{\mathrm{Ca}} \, w^0(\gamma^0_1)},$$

$$(3.70) \qquad \partial_t \gamma^0_1(t) = \frac{q(t)}{w^0(\gamma^0_1(t))}.$$

3.4. Hysteretic contact angle model.

The previous analysis requires that the dynamic contact angle relation is continuous, as expressed in (A5). However, experiments suggest the occurrence of contact angle hysteresis, see e.g. the reviews [10, 56] discussing this as a result of surface wettability and roughness. This means that static contact angles are not unique, but can vary due to pinning. Here, we allow that the contact angle relation θ^ε involves a multi-valued graph if the velocity of the contact line is zero. To still obtain a well-defined contact angle law, we reformulate the respective condition under the following assumption, which replaces (A5).

(A10) Restricted to $\mathbb{R} \setminus \{0\}$, θ^ε is a Lipschitz-continuous and strictly monotonic function into $(0, \pi)$. For a zero velocity, it can take any values as follows.

$$\theta^\varepsilon(0) \in \begin{cases} [\lim_{u \nearrow 0} \theta^\varepsilon(u), \lim_{u \searrow 0} \theta^\varepsilon(u)] & \text{if } \theta^\varepsilon \text{ is increasing,} \\ [\lim_{u \searrow 0} \theta^\varepsilon(u), \lim_{u \nearrow 0} \theta^\varepsilon(u)] & \text{otherwise.} \end{cases}$$

Using the monotonicity of θ^ε, one can invert the relation with respect to the velocity. For this, let $\zeta^\varepsilon := (\cos(\theta^\varepsilon))^{-1}$ be the inverse of $\cos \theta^\varepsilon$. By (A10), ζ^ε is well-defined and Lipschitz-continuous. As before, we assume that ζ^ε depends regularly on ε.

(A11) ζ^ε has a uniform expansion

$$\zeta^\varepsilon(a) = \zeta^0(a) + \varepsilon \zeta^1(a) + \mathcal{O}(\varepsilon^2),$$

where $\zeta^0 : (-1, 1) \to \mathbb{R}$ is Lipschitz-continuous.

With this, we study the Navier–Stokes system for two-phase flow (2.15)–(2.25), but replace (2.26) by the following, inverted contact angle condition

$$(3.71) \qquad \zeta^\varepsilon \left(\boldsymbol{t}^\varepsilon_\Gamma \big|_{s=1} \cdot \boldsymbol{t}^\varepsilon_{\mathrm{w}} \big|_{x_1 = \gamma^\varepsilon_1} \right) = \partial_t \gamma^\varepsilon_1.$$

Since the analysis in subsection 3.1 is independent of the interface region, and in particular does not use (A5) or the non-hysteretic contact angle relation (2.26), the derived bulk solutions (3.23)–(3.26) remain unchanged.

Using (A1)–(A4), (A6)–(A8) and (A11) instead of (A5), we repeat the analysis close to the interface $\Gamma^\varepsilon(t)$ from subsection 3.2. Following the same steps, we obtain a circular interface with constant curvature K^0, which is then implicitly given by

$$\partial_t \gamma_1^0 = \zeta^0 \left(w^0(\gamma_1^0) K^0 \right).$$

Combining this, the pressure balance (3.51), and the outer pressure solution (3.24) and (3.26), one obtains

$$(3.72) \qquad \partial_t \gamma_1^0 = \zeta^0 \left(w^0(\gamma_1^0) \overline{\mathrm{Ca}}(p_{\mathrm{in}}^0 - q J(\gamma_1^0)) \right),$$

where

$$J(\gamma_1^0) := \int_0^{\gamma_1^0} \frac{3}{(w^0(x_1))^2 (3\lambda^0 + w^0(x_1))} dx_1 + \int_{\gamma_1^0}^1 \frac{3\mathrm{M}}{(w^0(x_1))^2 (3\lambda^0 + w^0(x_1))} dx_1.$$

Together with (3.54), this forms a differential algebraic system of two equations for the two unknowns γ_1^0 and either p_{in}^0 or q. Furthermore, the Stokes problem for finding the velocity close to the interface remains unchanged as well.

The solution process depends again on the chosen inlet boundary condition, analogously to the discussion in subsection 3.2. As before, it is sufficient to obtain γ_1^0, p_{in}^0 and q, since these are the unknown coefficients for the bulk solutions $\boldsymbol{u}_m^0$ and p_m^0 ($m \in \{\mathrm{I}, \mathrm{II}\}$) given by (3.23)–(3.26). For an inlet velocity boundary condition $\boldsymbol{u}_{\mathrm{I}}^\varepsilon = \boldsymbol{u}_{\mathrm{in}}^\varepsilon$ (at $\Gamma_{\mathrm{in}}^\varepsilon$), the value of q is given. Hence, plugging this into (3.54) yields γ_1^0, and thus one can solve (3.72) for p_{in}^0. However, the solution of the inlet pressure p_{in}^0 is not unique if the contact angle relation θ^ε is multi-valued at velocity $u = 0$. On the other hand, for an inlet pressure condition $p_{\mathrm{I}}^\varepsilon = p_{\mathrm{in}}^\varepsilon$, the value of p_{in}^0 is known. Then, the differential algebraic system (3.54) and (3.72) has index 1 and can be solved for q and γ_1^0. A sufficient condition for the unique solvability is

$$(\zeta^0)' \left(w^0(\gamma_1^0) \overline{\mathrm{Ca}}(p_{\mathrm{in}}^0 - q J(\gamma_1^0)) \right) \neq \frac{1}{\overline{\mathrm{Ca}}(w^0(\gamma_1^0))^2 J(\gamma_1^0)}.$$

4. Averaged Models and Effective Quantities.

Based on the asymptotic solution for pressures and velocities, we continue with the study of averaged models and effective quantities. First, we show that a local, one-dimensional version of Darcy's law holds for the transversally averaged pressures and velocities. In the second part we derive effective quantities based on volume averages. The main result is a capillary pressure - saturation relationship involving dynamic effects.

In the following, we are only interested in the leading order relations. To simplify the notation, we therefore drop the indices $(\cdot)^\varepsilon$ and $(\cdot)^0$, and neglect higher-order terms. Hence, all following equations should be understood as up to terms of order ε.

4.1. Transversal average: Darcy's law.

In the following, we derive the transversal average of the quantities to demonstrate that the one-dimensional description of the thin strip yields a local version of Darcy's law. To this end, recall that the total flux (in the half strip) $q(t)$ is independent of x_1 as discussed in Remark 2.2. The transversally averaged velocity in x_1-direction is therefore given by

$$\bar{u}(t, x_1) := \begin{cases} (w(x_1))^{-1} \int_0^{w(x_1)} u_{1,\mathrm{I}}(t, \boldsymbol{x}) dx_2 & \text{for } x_1 < \gamma_1(t), \\ (w(x_1))^{-1} \int_0^{w(x_1)} u_{1,\mathrm{II}}(t, \boldsymbol{x}) dx_2 & \text{for } x_1 > \gamma_1(t). \end{cases}$$
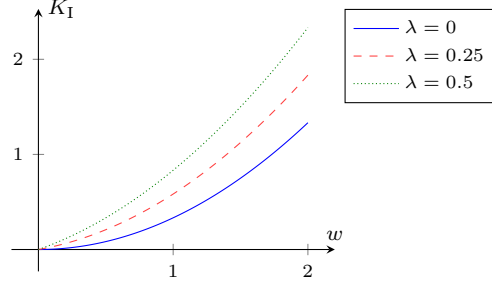
$$= \frac{q(t)}{w(x_1)}.$$

FIGURE 4.1. *The local permeability K_I has a quadratic dependence on the width w and increases for increasing slip length λ.*

Since the pressures p_{I} and p_{II} are independent of x_2, we obtain for the transversally averaged pressures

$$\bar{p}_{\text{I}}(t, x_1) := (w(x_1))^{-1} \int_0^{w(x_1)} p_{\text{I}}(t, \boldsymbol{x}) dx_2$$

$$= p_{\text{in}}(t) - q(t) \int_0^{x_1} \frac{3}{(w(\xi))^2(3\lambda + w(\xi))} d\xi \qquad \text{for } x_1 < \gamma_1(t),$$

$$\bar{p}_{\text{II}}(t, x_1) := (w(x_1))^{-1} \int_0^{w(x_1)} p_{\text{II}}(t, \boldsymbol{x}) dx_2$$

$$= q(t) \int_{x_1}^1 \frac{3\text{M}}{(w(\xi))^2(3\lambda + w(\xi))} d\xi \qquad \text{for } x_1 > \gamma_1(t).$$

This means that the transversally averaged pressures satisfy a Darcy-type law

$$\bar{u}(t, x_1) = -K_m(x_1)\partial_{x_1}\bar{p}_m(t, x_1)$$

for $m \in \{\text{I}, \text{II}\}$, where the local permeabilities are given by

$$K_{\text{I}}(x_1) := \tfrac{1}{3}w(x_1)(3\lambda + w(x_1)),$$

$$K_{\text{II}}(x_1) := \tfrac{1}{3\text{M}}w(x_1)(3\lambda + w(x_1)).$$

These permeabilities depend only on the local width w of the thin strip, on the slip length λ and on the viscosity ratio M of the fluids, see also Figure 4.1. Note that this resembles the typical relation $\bar{u} = \frac{d^2}{12}\partial_{x_1}p$ for single-phase flow in a thin strip of diameter $d = 2w$.

4.2. Effective quantities: Dynamic capillary pressure. To obtain effective quantities like the saturation and the intrinsically averaged pressures, we use volume averages. With these, we obtain a capillary pressure - saturation relationship involving dynamic effects. In line with classical volume averaging theory [73, 55], we define the volume average $\langle a_m \rangle$ of a quantity a_m defined in Ω_m, $m \in \{\text{I}, \text{II}\}$, to be

$$\langle a_m \rangle := \frac{\int_{\Omega_m} a_m d\boldsymbol{x}}{\int_\Omega d\boldsymbol{x}},$$

while the intrinsic average is

$$\langle a_m \rangle_m := \frac{\int_{\Omega_m} a_m d\boldsymbol{x}}{\int_{\Omega_m} d\boldsymbol{x}}.$$

The volume of the domain Ω_{I} is given by

$$\int_{\Omega_{\mathrm{I}}} d\boldsymbol{x} = \int_0^{\gamma_1} w(x_1)dx_1 = \mathcal{W}(\gamma_1).$$

Analogously, we have $\int_\Omega d\boldsymbol{x} = \mathcal{W}(1)$ and $\int_{\Omega_{\mathrm{II}}} d\boldsymbol{x} = \mathcal{W}(1) - \mathcal{W}(\gamma_1)$. Therefore, the saturation of fluid I is in leading order given by

$$(4.1) \qquad S(t) := \langle 1_{\Omega_{\mathrm{I}}(t)} \rangle = \frac{\int_{\Omega_{\mathrm{I}}(t)} d\boldsymbol{x}}{\int_\Omega d\boldsymbol{x}} = \frac{\mathcal{W}(\gamma_1(t))}{\mathcal{W}(1)}.$$

Note that we only consider the case when both phases are present, so that $\gamma_1(t) \in (0, 1)$ and $S \in (0, 1)$. For simplicity, we define the function

$$(4.2) \qquad \Psi(S) := \frac{1}{w(\mathcal{W}^{-1}(\mathcal{W}(1)S))},$$

which represents the reciprocal of the local width depending on the saturation S and on the geometry of the thin strip. Note that the system (3.53) and (3.54) can be rewritten in terms of the saturation as

$$p_{\mathrm{in}} - q\mathcal{W}(1) \left(\int_0^S \frac{3(\Psi(\xi))^3}{3\lambda + (\Psi(\xi))^{-1}} d\xi + \int_S^1 \frac{3\mathrm{M}(\Psi(\xi))^3}{3\lambda + (\Psi(\xi))^{-1}} d\xi \right)$$
$$= \frac{\cos(\theta(\mathcal{W}(1)\Psi(S)\partial_t S))}{\overline{\mathrm{Ca}}} \Psi(S),$$
$$\partial_t S = \frac{q}{\mathcal{W}(1)}.$$

However, this reformulation is less practical, since the function Ψ typically is not a closed-form expression.

Using (3.24), the intrinsically averaged pressure of fluid I is

$$\langle p_{\mathrm{I}} \rangle_{\mathrm{I}} = \frac{1}{\mathcal{W}(\gamma_1)} \int_0^{\gamma_1} w(x_1) \left(p_{\mathrm{in}} - q \int_0^{x_1} \frac{3}{(w(\xi))^2(3\lambda + w(\xi))} d\xi \right) dx_1,$$

which can be rewritten after integration by parts as

$$(4.3) \qquad \langle p_{\mathrm{I}} \rangle_{\mathrm{I}} = p_{\mathrm{I}}\big|_{x_1=\gamma_1} + \frac{3q}{\mathcal{W}(\gamma_1)} \int_0^{\gamma_1} \frac{\mathcal{W}(x_1)}{(w(x_1))^2(3\lambda + w(x_1))} dx_1.$$

Analogously, (3.26) yields the intrinsically averaged pressure of fluid II to be

$$(4.4) \qquad \langle p_{\mathrm{II}} \rangle_{\mathrm{II}} = p_{\mathrm{II}}\big|_{x_1=\gamma_1} - \frac{3\mathrm{M}q}{\mathcal{W}(1) - \mathcal{W}(\gamma_1)} \int_{\gamma_1}^1 \frac{\mathcal{W}(1) - \mathcal{W}(x_1)}{(w(x_1))^2(3\lambda + w(x_1))} dx_1.$$

Using the interface condition (3.53), the difference of the intrinsically averaged pressures, in the following called phase-pressure difference, is given by

$$(4.5) \qquad \langle p_{\mathrm{I}} \rangle_{\mathrm{I}} - \langle p_{\mathrm{II}} \rangle_{\mathrm{II}} = \frac{\cos(\theta(\partial_t \gamma_1))}{\overline{\mathrm{Ca}} w(\gamma_1)} + 3q \left(\frac{1}{\mathcal{W}(\gamma_1)} \int_0^{\gamma_1} \frac{\mathcal{W}(x_1)}{(w(x_1))^2(3\lambda + w(x_1))} dx_1 \right.$$
$$\left. + \frac{\mathrm{M}}{\mathcal{W}(1) - \mathcal{W}(\gamma_1)} \int_{\gamma_1}^1 \frac{\mathcal{W}(1) - \mathcal{W}(x_1)}{(w(x_1))^2(3\lambda + w(x_1))} dx_1 \right).$$

Using (4.1) and (4.2) and the interface condition (3.54), this difference can be expressed in the form

$$\langle p_{\mathrm{I}}\rangle_{\mathrm{I}} - \langle p_{\mathrm{II}}\rangle_{\mathrm{II}} = p_{c,\mathrm{loc}}(S, \partial_t S) + \tau(S)\partial_t S. \tag{4.6}$$

The first term on the right denotes the local capillary pressure $p_{c,\mathrm{loc}} := (p_{\mathrm{I}} - p_{\mathrm{II}})|_{x_1=\gamma_1}$ given by

$$p_{c,\mathrm{loc}}(S, \partial_t S) = \frac{\cos(\theta(\mathcal{W}(1)\Psi(S)\partial_t S))}{\overline{\mathrm{Ca}}}\Psi(S). \tag{4.7}$$

The second term in (4.6) can be interpreted as a dynamic capillarity due to the viscous drag. In particular, its coefficient is

$$\tau(S) = \frac{3\mathcal{W}(1)}{S}\int_0^S \frac{\xi(\Psi(\xi))^3}{3\lambda + (\Psi(\xi))^{-1}}d\xi + \frac{3\mathcal{W}(1)\mathrm{M}}{1-S}\int_S^1 \frac{(1-\xi)(\Psi(\xi))^3}{3\lambda + (\Psi(\xi))^{-1}}d\xi, \tag{4.8}$$

which depends on the slip length λ, the viscosity ratio M and the wall function w. Note that under static conditions, when $q \ll 1$, we have $p_{\mathrm{in}} \approx \langle p_{\mathrm{I}}\rangle_{\mathrm{I}} - \langle p_{\mathrm{II}}\rangle_{\mathrm{II}} = p_{c,\mathrm{loc}}$, such that the measurement of the inlet pressure yields (static) capillary pressure–saturation relation, but under the dynamic conditions studied here, these quantities can considerably differ. This one must be aware of when performing experiments.

The local capillary pressure $p_{c,\mathrm{loc}}$ depends reciprocally on the effective capillary number $\overline{\mathrm{Ca}}$ and on the local width $w(\mathcal{W}^{-1}(\mathcal{W}(1)S)) = 1/\Psi(S)$ of the thin strip. In case of a dynamic contact angle model of the form $\cos(\theta(u)) = \cos(\theta_s) + \eta\overline{\mathrm{Ca}}u$, the molecular kinetic theory in [9, 10], (4.7) yields

$$p_{c,\mathrm{loc}}^{\mathrm{MKT}}(S, \partial_t S) = \frac{\cos(\theta_s)}{\overline{\mathrm{Ca}}}\Psi(S) + \eta\mathcal{W}(1)(\Psi(S))^2\partial_t S. \tag{4.9}$$

The static and dynamic effects are decoupled in this case. The first term models the static (local) capillary pressure, while the second term is a dynamic contribution.

In case of a constant contact angle $\theta \equiv \theta_s \in (0, \pi)$, (4.7) yields the local capillary pressure

$$p_{c,\mathrm{loc}}^{\mathrm{const}}(S) = \frac{\cos(\theta_s)}{\overline{\mathrm{Ca}}}\Psi(S).$$

With $l(t) := \int_{\Gamma_{\boldsymbol{x}}(t)} ds$ being the length of the circular interface $\Gamma_{\boldsymbol{x}}(t)$ at time t, the local capillary pressure becomes

$$p_{c,\mathrm{loc}}^{\mathrm{const}}(l) = \frac{\frac{\pi}{2} - \theta_s}{\overline{\mathrm{Ca}}\,l}.$$

Observe that $l(t)$ can be assimilated to the interfacial area concept considered in [29, 30]. Note that for a dynamic contact angle, there is no simple closed-form expression of the local capillary pressure as a function of the interface length (nor of its derivatives).

5. Numerical Experiments. To illustrate the theoretical findings, we depict some numerical examples in this section. We start with a thin strip of constant width, and afterwards consider a constricted "pore throat" with varying width. After a short discussion of the boundary conditions, we consider the resulting effective quantities. In particular, we study the effect of the slip length and the viscosity ratio and discuss the effect of a dynamic and a hysteretic contact angle model for both geometries.

We have implemented the numerical solutions using MATLAB® R2020a [66]. The source code is available under the CC-BY license at https://github.com/s-lunowa/AsymptoticThinStripMCLSolver.

Parameter		Value
Capillary number	$\overline{\mathrm{Ca}}$	$1/2$
Contact angle	θ	$\pi/3$
Slip length	λ	$1/6$
Viscosity ratio	M	1
Initial interface position	$\gamma_1\vert_{t=0}$	0
Inlet pressure	p_{in}	3

TABLE 5.1

Standard parameters for the thin strip of constant width.
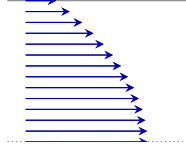
FIGURE 5.1. *Velocity profile in the thin strip with constant width ($\lambda = 1/6$).*

5.1. Thin strip of constant width. First we consider a simple case, which is a thin strip of constant width $w^\varepsilon \equiv 1$, and study the velocity and pressure distribution of the two phases as well as the movement of the interface. After a short discussion of the effect of different inlet boundary conditions, we will consider the effect of different parameter choices in the following subsections — the slip length in subsection 5.1.1, the viscosity ratio in subsection 5.1.2, and dynamic and hysteretic contact angle models in subsections 5.1.3 and 5.1.4, respectively. Except for the varying parameter mentioned in each subsection, all the other ones are fixed, as given in Table 5.1. In particular, the contact angle model considered when discussing the other parameters is constant, i.e., the contact angle is static and fluid I is non-wetting.

For this geometry, the solution given in (3.23)–(3.26) for the bulk domains becomes

$$(5.1)\quad \boldsymbol{u}_{\mathrm{I}}(t,\boldsymbol{x}) = \begin{pmatrix} 3q(t)\frac{2\lambda+1-x_2^2}{6\lambda+2} \\ 0 \end{pmatrix}, \quad p_{\mathrm{I}}(t,\boldsymbol{x}) = p_{\mathrm{in}}(t) - q(t)\frac{3x_1}{3\lambda+1}, \quad \text{for } x_1 < \gamma_1(t),$$

$$(5.2)\quad \boldsymbol{u}_{\mathrm{II}}(t,\boldsymbol{x}) = \begin{pmatrix} 3q(t)\frac{2\lambda+1-x_2^2}{6\lambda+2} \\ 0 \end{pmatrix}, \quad p_{\mathrm{II}}(t,\boldsymbol{x}) = q(t)\frac{3\mathrm{M}(1-x_1)}{3\lambda+1}, \quad \text{for } x_1 > \gamma_1(t).$$

This means that the velocity profiles are of Hagen-Poiseuille type, see also Figure 5.1. The pressures decrease linearly inside the bulk phases due to the viscous forces. Furthermore, the interface system (3.53) and (3.54) simplifies into

$$(5.3)\qquad p_{\mathrm{in}}(t) - q(t)\frac{3\gamma_1(t) + 3\mathrm{M}(1-\gamma_1(t))}{3\lambda+1} = \frac{\cos(\theta(q(t)))}{\overline{\mathrm{Ca}}}, \quad \partial_t\gamma_1(t) = q(t).$$

The actual size of the quantities and the movement of the interface depends on the inlet boundary conditions, on the effective capillary number, on the slip length, on the viscosity ratio and on the contact angle model. Here, we shortly discuss the qualitatively different cases with respect to the inlet boundary conditions and the viscosity ratio, when all other parameters are given by Table 5.1 for simplicity.

(a) When the inlet velocity is fixed, e.g. $u_{\mathrm{in},1} = 4/3 - x_2^2$, one obtains $q(t) = 1$ and thus the constant (in time) velocities $u_{m,1} = 4/3 - x_2^2$ for $m \in \{\mathrm{I}, \mathrm{II}\}$, so that the

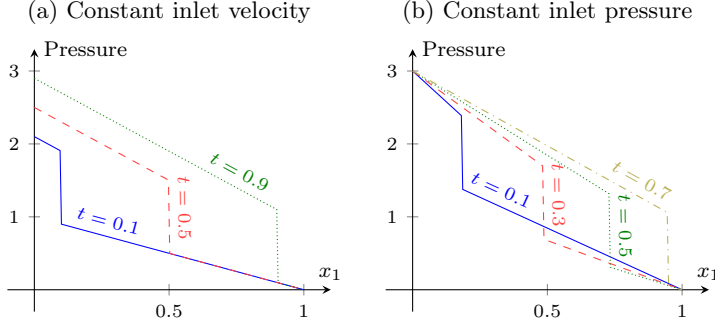(a) Constant inlet velocity   (b) Constant inlet pressure

FIGURE 5.2. *Pressure distribution over length x_1 at various times in the thin strip of constant width for viscosity ratio $M = 0.5$. The solution depends on the inlet boundary condition and shows a more dynamic behaviour in case (b) than in case (a).*

interface moves linearly, $\gamma_1(t) = t$. The pressures are then given by

$$p_I(t, \boldsymbol{x}) = 1 + 2M + 2(1 - M)t - 2x_1, \qquad p_{II}(t, \boldsymbol{x}) = 2M(1 - x_1).$$

For $M \neq 1$, the pressure of fluid I is time-dependent, see also Figure 5.2, while both pressures are constant in time for $M = 1$.

(b) When the inlet pressure is fixed, e.g. $p_{in} = 3$, the flow of both fluids is time-dependent. For a viscosity ratio $M < 1$, one obtains the solution

$$p_I(t, \boldsymbol{x}) = 3 - \frac{2(1-M)x_1}{\sqrt{M^2 + 2(1-M)t}}, \qquad p_{II}(t, \boldsymbol{x}) = \frac{2M(1-M)(1-x_1)}{\sqrt{M^2 + 2(1-M)t}},$$

$$u_{m,1}(t, \boldsymbol{x}) = \frac{(1-M)\left(\frac{4}{3} - x_2^2\right)}{\sqrt{M^2 + 2(1-M)t}}, \qquad \gamma_1(t) = \frac{\sqrt{M^2 + 2(1-M)t} - M}{1 - M},$$

for $m \in \{I, II\}$, see Figure 5.2. Analogous behaviour can be observed when $M > 1$. Only for $M = 1$, both pressures are constant in time, like in (a).

From these examples, we observe a more dynamic behaviour when the inlet pressure is given, which corresponds also to the typical setting for capillary pressure experiments. Thus, we restrict the following discussion to the case of given pressure boundary condition at the inlet.

Due to the constant width, the effective quantities have rather simple algebraic expressions. The saturation S coincides with the interface position, i.e., $S = \gamma_1$. The local permeabilities are constant and given by

$$(5.4) \qquad K_I \equiv \frac{1 + 3\lambda}{3}, \qquad\qquad K_{II} \equiv \frac{1 + 3\lambda}{3M}.$$

The local capillary pressure, the dynamic coefficient and the phase-pressure difference are

$$(5.5) \qquad p_{c,\text{loc}}(S, \partial_t S) = \frac{\cos\theta(\partial_t S)}{\overline{Ca}}$$

$$(5.6) \qquad \tau(S) = 3\frac{S + M(1 - S)}{6\lambda + 2},$$

$$(5.7) \qquad \langle p_I \rangle_I - \langle p_{II} \rangle_{II} = \frac{p_{in} + p_{c,\text{loc}}(S, \partial_t S)}{2}.$$
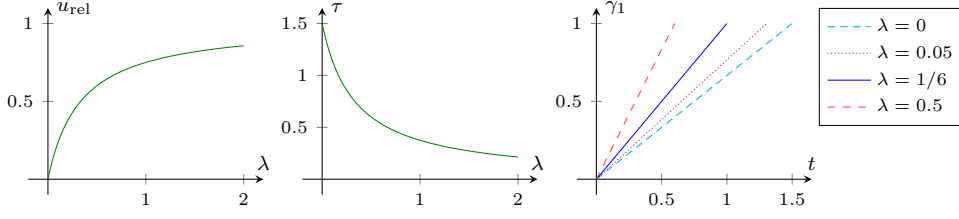
FIGURE 5.3. *For an increasing slip length λ, the velocity ratio $u_{rel} = u_{m,1}\big|_{x_2=1}/q$ at the wall increases (left), while the dynamic parameter τ decreases (center). The interface position γ_1 moves faster for an increasing slip length λ (right).*

As direct consequence of the constant contact angle in Table 5.1, we obtain a constant local capillary pressure $p_{c,\text{loc}} \equiv 1$ by (5.5) and a constant phase-pressure difference $\langle p_{\text{I}} \rangle_{\text{I}} - \langle p_{\text{II}} \rangle_{\text{II}} \equiv 2$ by (5.7). Changing the static contact angle $\theta \equiv \theta_s \in (0, \pi)$ or the capillary number $\overline{\text{Ca}}$ influences the size of the local capillary pressure and the size of the phase-pressure difference in a straightforward way, while the behaviour of the other quantities remains qualitatively the same. For simplicity, we do not discuss their detailed effects. Note that $p_{c,\text{loc}}$ and $\langle p_{\text{I}} \rangle_{\text{I}} - \langle p_{\text{II}} \rangle_{\text{II}}$ do not depend on the slip length nor on the viscosity ratio. Hence, we only consider their behaviour for dynamic and hysteretic contact angle models. Meanwhile, the dynamic coefficient depends on the slip length and the viscosity ratio, which is relevant in case of a inlet velocity condition.

5.1.1. Effect of the slip length. First, we consider the effect of the slip length λ while using all other parameters as above. The velocity at the wall is given by

$$u_{m,1}\big|_{x_2=1} = q\tfrac{3\lambda}{3\lambda+1} \qquad \text{for } m \in \{\text{I}, \text{II}\}.$$

It is zero for $\lambda = 0$, increases for an increasing slip length, and approaches q for $\lambda \to \infty$, which corresponds to a total slip, see Figure 5.3. This is a result of the decreased friction of the fluid at the wall for an increased slip length. Additionally, this leads to a smaller dynamic coefficient τ, cf. (5.6) and Figure 5.3. For constant inlet pressure, the decrease of the pressure gradients in (5.1) and (5.2) for an increased slip length λ are compensated by a larger total flux q, and thus a faster movement of the interface position γ_1, see also Figure 5.3. The local permeabilities K_{I}, K_{II} show a similar behaviour. Observe that since $w \equiv 1$, these only depend on the slip length. As follows from (5.4) (see also Figure 4.1), they increase linearly with λ.

5.1.2. Effect of the viscosity ratio. Next, we continue the investigation for various viscosity ratios M. Since the viscous force in fluid II is proportional to the viscosity ratio M, the total flux q decreases when the viscosity ratio M increases, cf. (5.3). In particular, the interface position γ_1 moves faster when the thin strip is mainly filled by the less viscous fluid. Furthermore, we observe that the solutions converge for M $\to 0$ towards solution of the simplified, unsaturated flow model as discussed in subsection 3.3, see Figure 5.4. Note that we use $\gamma_1|_{t=0} = 10^{-3}$ when M $= 0$ to avoid the degeneration of the interface system (5.3).

The dynamic coefficient τ becomes larger for small saturations S, if the viscosity ratio is large (M > 1), and vice versa for M < 1, see (5.6) and Figure 5.4. Note that one can observe even in this extremely simplified setting that the dynamic coefficient is
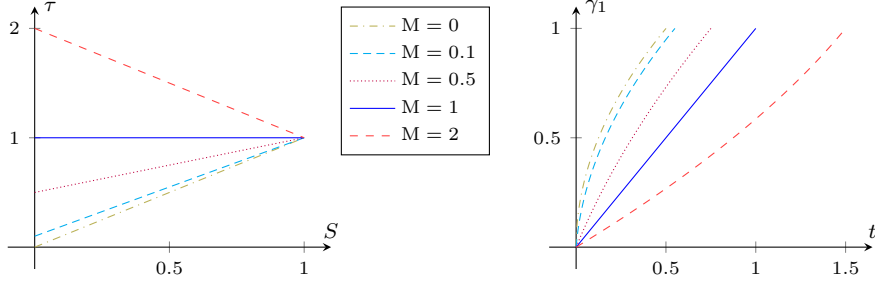
FIGURE 5.4. *For increasing viscosity ratio M, the dynamic parameter τ increases (left), while the interface position γ_1 moves slower (right).*
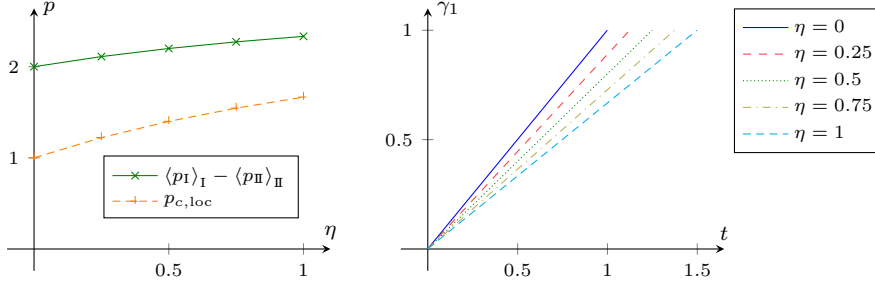

FIGURE 5.5. *The local capillary pressure $p_{c,loc}$ increases for increasing dynamic contact angle coefficient η (left). Hence, the movement of the interface position γ_1 slows down (right).*

saturation dependent, except for fluids with the same viscosity (M = 1). Additionally, the dynamic coefficient is monotonic in the saturation S for any viscosity ratio.

5.1.3. Effect of a dynamic contact angle. Now, we consider the effect of a dynamic contact angle model. As we expect the similar qualitative behaviour for different dynamic contact angle models, we restrict the discussion to the model

$$(5.8) \qquad \theta(u) = \arccos(\max(\min(\cos(\theta_s) + \eta\overline{\mathrm{Ca}}u, 1), -1)),$$

which is the molecular kinetic theory model from [11, 15, 9, 10] restricted to the possible range $[0, \pi]$. Here, the parameter $\eta \geq 0$ models the effective friction at the contact point leading to a dynamic contact angle. For comparability, we fix the static contact angle $\theta_s = \pi/3$ and all the other parameters as in Table 5.1. Note that for any $\eta \geq 0$, the differential algebraic system (5.3) has a unique solution, since cosine is monotonic decreasing on $[0, \pi]$.

In contrast to the previous examples, the dynamic contact angle model does not affect the dynamic coefficient τ, but has an impact on the local capillary pressure $p_{c,\mathrm{loc}}$ and the phase-pressure difference $\langle p_{\mathrm{I}} \rangle_{\mathrm{I}} - \langle p_{\mathrm{II}} \rangle_{\mathrm{II}}$. Recall that the local capillary pressure is given in this case by (4.9). In particular, its dynamic part is proportional to the parameter η. Hence, the interface position γ_1 moves slower when the parameter η increases, see Figure 5.5. Note that the total flux q is constant, so that γ_1 is linear in time. Therefore, the local capillary pressure and the phase-pressure difference are constant over S (due to M = 1), so that we only show the dependence on η in Figure 5.5.
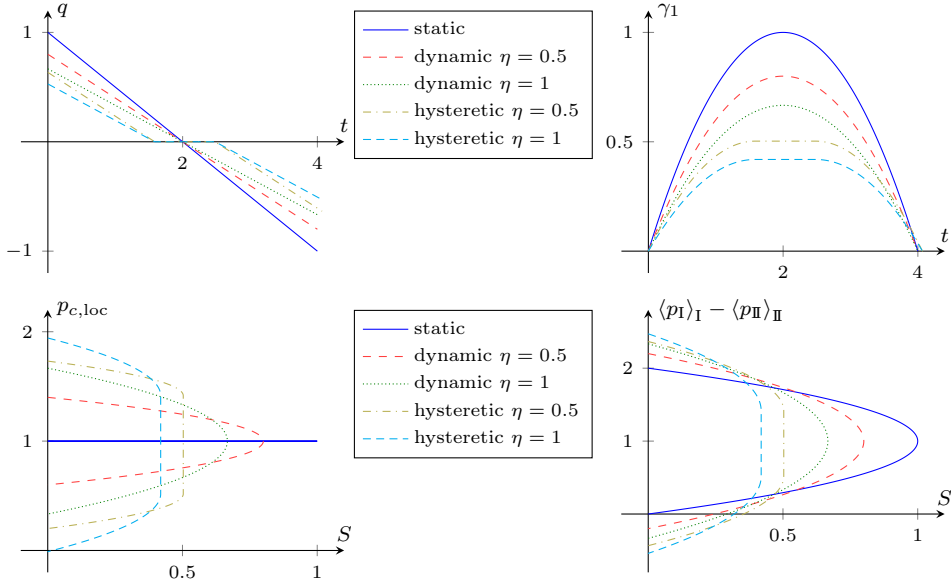
FIGURE 5.6. *The total flux q (top-left) is linear for the static and dynamic contact angle model, while being zero for some time for the hysteretic model. The interface position γ_1 moves accordingly (top-right). In case of the hysteretic model, it is at rest, when the local capillary pressure $p_{c,loc}$ (bottom-left) lies in between the (static) capillary pressures for drainage and imbibition, i.e., $p_{c,loc}$ is multi-valued at the maximal reached saturation. For the dynamic models, $p_{c,loc}$ at the maximal saturation is exactly the static capillary pressure. The phase-pressure difference $\langle p_I \rangle_I - \langle p_{II} \rangle_{II}$ (bottom-right) shows the same qualitative behaviour.*

5.1.4. Effect of a hysteretic contact angle. Finally, we consider the effect of a hysteretic contact angle model and compare it to the static and dynamic ones. As before we use the dynamic contact angle model (5.8) with static contact angle $\theta_s = \pi/3$. For the hysteretic contact angle model, the advancing and receding contact angles (with respect to fluid I) are chosen $\theta_a = \pi/4$ and $\theta_r = 5\pi/12$, respectively. Together with the same dynamic contact angle model away from $u = 0$, this yields

$$(5.9) \qquad \zeta(a) = \begin{cases} \frac{a - \cos(\theta_r)}{\eta \overline{Ca}} & \text{if } a < \cos(\theta_r), \\ \frac{a - \cos(\theta_a)}{\eta \overline{Ca}} & \text{if } a > \cos(\theta_a), \\ 0 & \text{otherwise.} \end{cases}$$

Recall that ζ is the inverse of $\cos \theta$. We consider a drainage and imbibition cycle by choosing the time-dependent inlet pressure $p_{in}(t) = 3 - t$, and stop the simulations when the interface position returns to the inlet. The other parameters are taken from Table 5.1.

As in the dynamic case, we observe that the movement of the interface position γ_1 is slower when the parameter η is increased, see Figure 5.6 (top). While the total flux q is linear for the static and dynamic contact angle model, so that γ_1 is quadratic in time, the hysteretic model leads to a constant interface position when $\theta_a \leq \theta \leq \theta_r$. Therefore, the local capillary pressure $p_{c,loc}$ and the phase-pressure difference $\langle p_I \rangle_I - \langle p_{II} \rangle_{II}$ at the maximal reached saturation is multi-valued taking all values between the (static) drainage and imbibition capillary pressures, see Figure 5.6 (bottom). On the other hand, for the dynamic contact angle model, $p_{c,loc}$ and $\langle p_I \rangle_I -$

Parameter		Value
Capillary number	$\overline{\mathrm{Ca}}$	$1/2$
Contact angle	θ	$\pi/3$
Slip length	λ	$1/6$
Viscosity ratio	M	1
Initial interface position	$\gamma_1|_{t=0}$	0
Inlet pressure	p_{in}	12

TABLE 5.2

Standard parameters for the case of varying width.
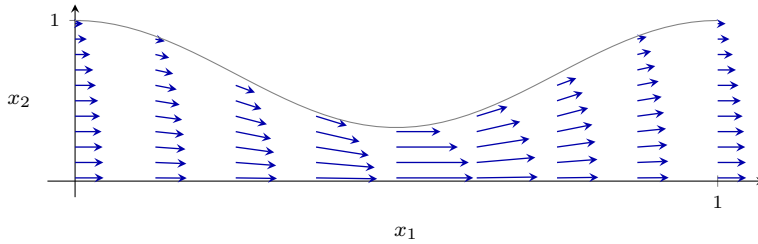
FIGURE 5.7. *Velocity profile in the thin strip of varying width ($\lambda = 1/6$).*

$\langle p_{\mathbb{I}} \rangle_{\mathbb{I}}$ at the maximal saturation are given by the static capillary pressure, since $\partial_t S = 0$. Furthermore, the hysteresis leads to higher deviations from the static capillary pressure and thus a smaller maximal saturation. Finally, note that p_{in} is linear and reaches $p_{c,\mathrm{loc}}^{\mathrm{const}}$ at $t = 2$ such that all curves with the dynamic contact angle model are symmetric. Since θ_a and θ_r have the same distance from θ_s, the same holds in the hysteretic cases.

5.2. Constricted "pore throat". Next, we consider a strip with varying width

$$w(x_1) = 2/3 + \cos(2\pi x_1)/3,$$

which represents a constricted "pore throat". As before, we shortly discuss the velocity and pressure distribution of the two phases as well as the movement of the interface, before proceeding with the detailed discussion of the effect of the slip length, of the viscosity ratio and of a dynamic and a hysteretic contact angle model, varying each individually, while fixing all other parameters as given in Table 5.2. Note that we choose a static contact angle such that fluid I is non-wetting.

While the overall trend is similar to the previous case with constant width, we additionally observe here a strong impact of the geometry on the flow behaviour and thus on the effective quantities. In contrast to the constant-width case, the local capillary pressure $p_{c,\mathrm{loc}}$ now depends on the saturation due to the constriction, see Figure 5.9. Analogously, the phase-pressure difference $\langle p_{\mathrm{I}} \rangle_{\mathrm{I}} - \langle p_{\mathbb{I}} \rangle_{\mathbb{I}}$ varies in the saturation.

The solution in the bulk domains (3.23)–(3.26) for this geometry then reads

$$u_{m,1}(t, \boldsymbol{x}) = 9q(t) \frac{(c(x_1))^2 + 5c(x_1) + 6 - x_2^2}{(c(x_1) + 2)^2 (2c(x_1) + 7)},$$

$$u_{m,2}(t, \boldsymbol{x}) = \varepsilon 18\pi q(t) \sin(2\pi x_1) \left(\frac{18(c(x_1)+3)x_2^3}{(c(x_1)+2)^3(2c(x_1)+7)^2} - \frac{(2(c(x_1))^2 + 12c(x_1) + 19)x_2}{(c(x_1)+2)^2(2c(x_1)+7)^2} \right),$$
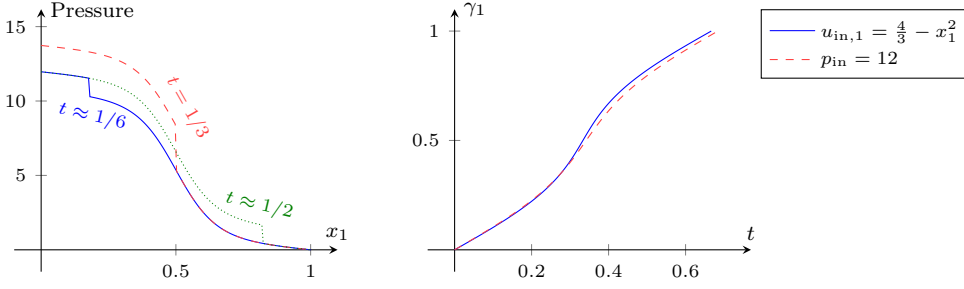
FIGURE 5.8. *Pressure distribution over length x_1 at various times (left) for fixed inlet velocity $u_{in,1} = 4/3 - x_1^2$ and interface position γ_1 over time t (right) for fixed inlet velocity $u_{in,1} = 4/3 - x_1^2$ and fixed pressure condition $p_{in} = 12$ in the thin strip of varying width.*
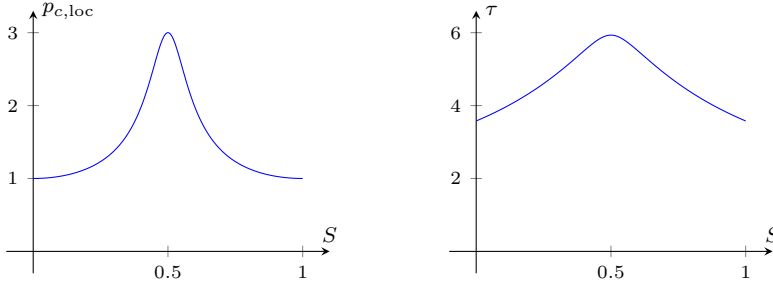

FIGURE 5.9. *The local capillarity pressure $p_{c,loc}$ increases for saturations below $S = 0.5$, and decreases thereafter. The dynamic coefficient τ shows an analogous behaviour. This is a result of the symmetric constriction of the thin strip.*

for $m \in \{\text{I}, \text{II}\}$, where $c(x_1) := \cos(2\pi x_1)$, see also Figure 5.7, while

$$p_{\text{I}}(t, \boldsymbol{x}) = \frac{3}{2 + c(\gamma_1(t))} + \frac{9q(t)\sin(2\pi x_1)}{\pi(c(x_1) + 2)} + \frac{24q(t)\left(\pi H(0.5 - x_1) - \arctan\left(\frac{\sqrt{5}}{3}\tan(\pi x_1)\right)\right)}{\pi\sqrt{5}},$$

for $x_1 < \gamma_1(t)$, and

$$p_{\text{II}}(t, \boldsymbol{x}) = \frac{9q(t)\sin(2\pi x_1)}{\pi(c(x_1) + 2)} + \frac{24q(t)\left(\pi H(0.5 - x_1) - \arctan\left(\frac{\sqrt{5}}{3}\tan(\pi x_1)\right)\right)}{\pi\sqrt{5}},$$

for $x_1 > \gamma_1(t)$, where H denotes the Heaviside graph, see also Figure 5.8. The first velocity component is higher where the width is reduced, while the second component adjusts to the changes in width to maintain the incompressibility, see Figure 5.7. Note that the second velocity component is of order ε due to the different scaling. Accordingly, the pressure gradients depend on the local width and are steeper around the constriction in the middle. This leads to the s-shaped pressure profiles instead of the linear ones in the constant-width case.

For fixed inlet velocity $u_{\text{in},1} = 4/3 - x_2^2$, i.e., for $q \equiv 1$, the pressure solutions at several times are depicted in Figure 5.8 together with the evolution of the interface position $\gamma_1(t)$, which is given implicitly by $t = 2\gamma_1(t)/3 + \sin(2\pi\gamma_1(t))/(6\pi)$. Note that the interface position γ_1 moves faster in the vicinity of the constriction, since the average velocity $\overline{u} = q/w$ is higher around the constriction, cf. Figure 5.7. Furthermore, the movement is very similar to the one obtained with constant inlet pressure $p_{\text{in}} \equiv 12$. Hence, we restrict the following discussion to this inlet pressure condition.
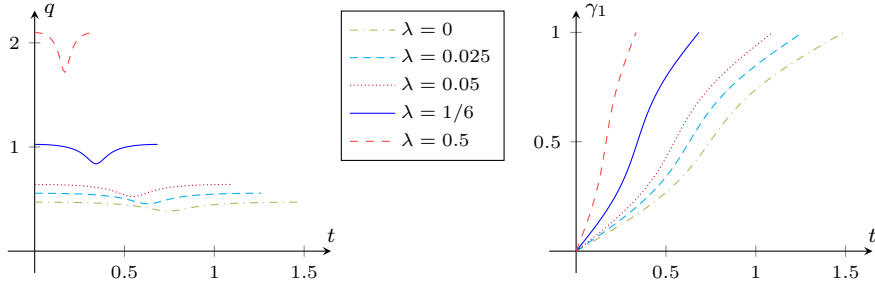
FIGURE 5.10. *The total flux q (left) is drastically reduced while the interface passes through the constriction due to the larger capillary pressure. It increases when the slip length λ is increased, so that the movement of the interface position γ_1 is faster (right).*
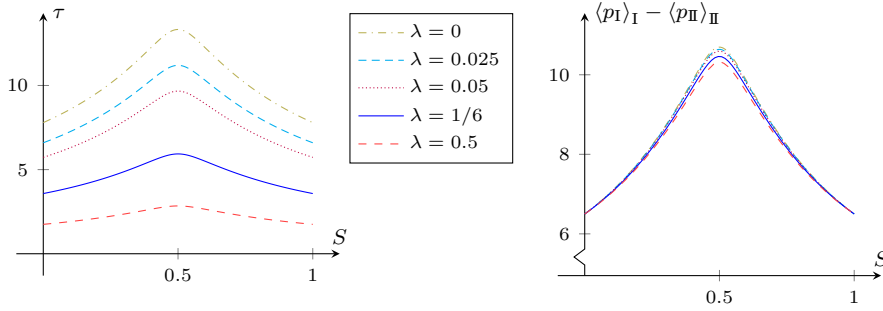

FIGURE 5.11. *The dynamic coefficient τ decreases for increasing slip length λ (left). It is non-monotonic in the saturation. The resulting phase-pressure difference $\langle p_I \rangle_I - \langle p_{II} \rangle_{II}$ is also non-monotonic, but almost the same for all slip lengths (right).*

Note that this larger inlet pressure is necessary to obtain a similar total flux as in the constant-width case, since the width is reduced.

For this geometry, we still can derive relations for the effective quantities obtained in subsection 4.2. We obtain for the saturation

$$S = \gamma_1 + \tfrac{1}{4\pi} \sin(2\pi\gamma_1), \qquad \partial_t S = \tfrac{3}{2} q.$$

Since this function $S(\gamma_1)$ has no analytical inverse, there is no closed-form expression for the local capillary pressure $p_{c,\text{loc}}$ (4.7) nor for the dynamic coefficient τ (4.8). Their numeric approximations are depicted in Figure 5.9. Both have a peak at $S = 0.5$, where the interface passes the position $x_1 = 0.5$ with the smallest width. For the local capillary pressure this results from the reciprocal dependence on the local width, while the dynamic coefficient is symmetric due to the symmetric wall and the viscosity ratio M = 1. Note that the dynamic effects are much stronger than in the constant-width setting due to the reduced width, which requires larger pressure gradients to maintain the flow. Hence, we conclude that the wall shape has a significant impact, especially on the dynamic effects.

5.2.1. Effect of the slip length. We begin the investigation for various slip lengths λ. As in the previous, constant-width case, the movement of the interface position γ_1 is faster when the slip length is increased, see Figure 5.10. However, the total flux q is drastically reduced while the interface passes through the constriction due to the higher capillary pressure, cf. Figure 5.10.
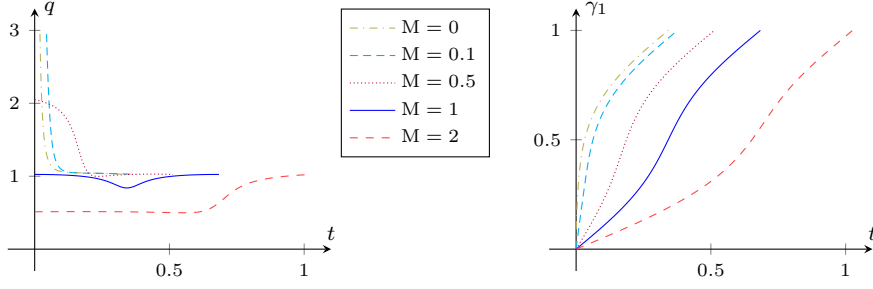
FIGURE 5.12. *The total flux q (left) is high when the thin strip is mainly filled with the less viscous fluid. It is smaller while the interface passes through the constriction. When the viscosity ratio M is increased, the interface position γ_1 moves generally slower (right).*
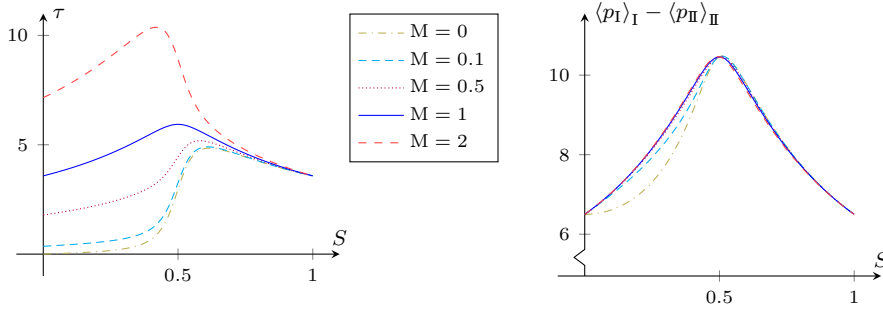

FIGURE 5.13. *The dynamic parameter τ increases for increasing viscosity ratio M (left). It is non-monotonic in the saturation. The resulting phase-pressure difference $\langle p_I \rangle_I - \langle p_{II} \rangle_{II}$ is also non-monotonic, but almost the same for all moderate viscosity ratios (right).*

The dynamic coefficient τ is lower when the slip length increases, as shown in Figure 5.11. In contrast to the constant-width case, it is non-monotonic in the saturation, and maximal around $S = 0.5$, i.e., when the interface passes through the constriction around $x_1 = 0.5$. Note that the combination of higher velocity with lower dynamic coefficient leads to almost no changes in the phase-pressure difference $\langle p_I \rangle_I - \langle p_{II} \rangle_{II}$ for all slip lengths, see Figure 5.11.

5.2.2. Effect of the viscosity ratio. Next, we consider the effect of the viscosity ratio M. As in the previous, constant-wall case, the total flux q is smaller when the viscosity ratio M increases, see also Figure 5.12. Especially at early times t, one can observe large total fluxes q, when the viscosity ratio is very small (M $\leq$ 0.1), since the strip is filled with the extremely mobile fluid II. On the other hand, the total flux is reduced while the interface passes through the constriction, but this effect is very small compared to the effect of viscosity for M $<$ 1. As before, the solutions converge for M $\to$ 0 towards the simplified, unsaturated flow model as discussed in subsection 3.3, see Figure 5.12. Note that we use $\gamma_1 \big|_{t=0} = 10^{-3}$ when M $= 0$ to avoid the degeneration of the interface system (3.53) and (3.54).

The dynamic coefficient τ becomes larger for small saturations S, if the viscosity ratio is larger (M $>$ 1), and vice versa for M $<$ 1, as shown in Figure 5.13. The rapid change close to $S = 0.5$ is due to the strong influence of the region around $x_1 = 0.5$, where the thin strip has its minimal width. Note that for small viscosity ratio M $\leq$ 0.1 and saturation below 0.4, the dynamic coefficient is almost zero. Furthermore, we
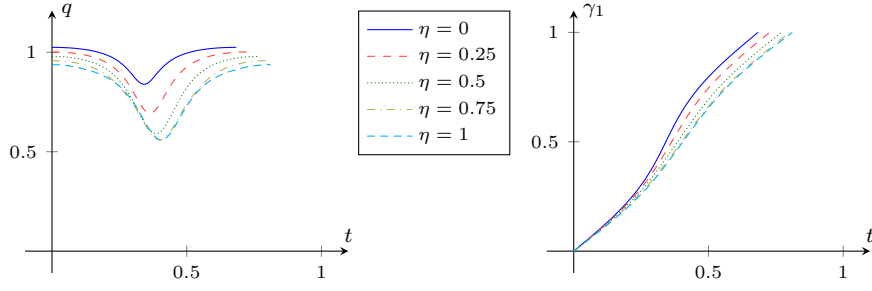
FIGURE 5.14. *The total flux q (left) decreases for higher values of η, since the (dynamic) local capillary pressure increases. Accordingly, the interface position γ₁ moves slower (right). Due to the constriction, the effect is maximal for γ₁ = 0.5.*
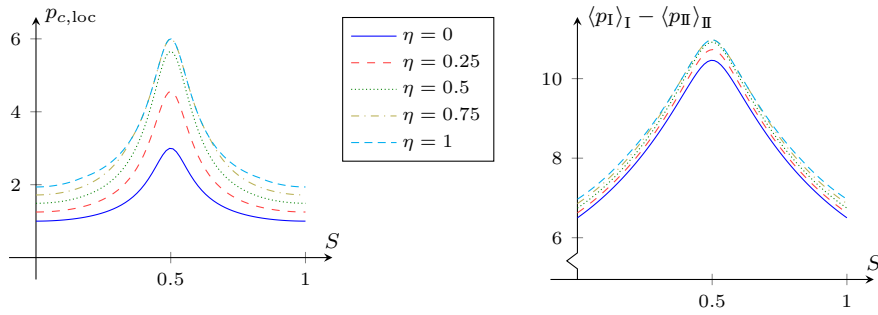

FIGURE 5.15. *The local capillary pressure $p_{c,loc}$ increases for increasing dynamic contact angle coefficient η (left). It attains its maximum at $S = 0.5$, when the interface passes the minimal width. The resulting phase-pressure difference $\langle p_I \rangle_I - \langle p_{II} \rangle_{II}$ shows the same behaviour (right).*

observe here non-monotonic behaviour of the dynamic coefficient τ for every viscosity ratio, while it is monotonic in the constant-width case. This is due to the interplay between the constricted geometry and the nonlinear dynamic effect (4.8). Finally, note that the combination of higher velocity with lower dynamic coefficient leads to almost no changes in the phase-pressure difference $\langle p_I \rangle_I - \langle p_{II} \rangle_{II}$ for all moderate viscosity ratios, see Figure 5.13. Only for a very small viscosity ratio M ≤ 0.1, the phase-pressure difference is slightly lower for saturations between 0 and 0.5.

5.2.3. Effect of a dynamic contact angle. We consider the effect of a dynamic contact angle model. As for the constant-width case, we use (5.8) with $\theta_s = \pi/3$. The total flux q is smaller when η is increased, see Figure 5.14. This effect is amplified while the interface passes through the constriction.

Although the total flux is smaller, the local capillary pressure $p_{c,loc}$ and the phase-pressure difference $\langle p_I \rangle_I - \langle p_{II} \rangle_{II}$ increase for increasing η, see Figure 5.15. The maximum is attained at $S = 0.5$, when the interface passes the minimal width. There, the dynamic effect is also the highest. Note that the curves for $\eta = 0.75$ and $\eta = 1$ partly coincide because the dynamic contact angle reaches π in both cases. In a laboratory experiment, this could lead to instabilities and the formation of bubbles or a thin residual film. However, that such behaviour is beyond the scope of the model presented here.
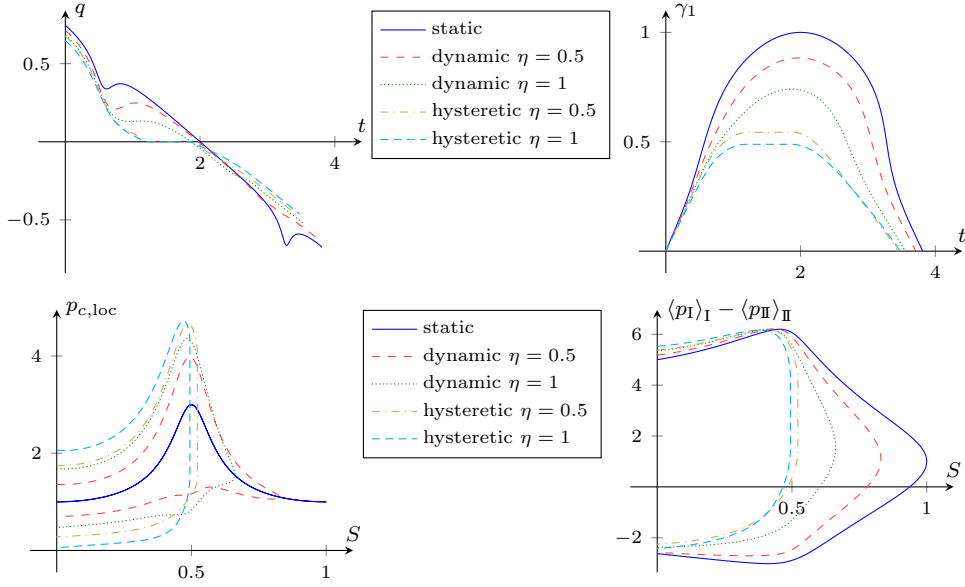
FIGURE 5.16. *The total flux q (top-left) decreases faster when the interface passes through the constriction. In case of the hysteretic contact angle model the interface position γ_1 (top-right) stops in the constriction when the local capillary pressure $p_{c,loc}$ (bottom-left) lies in between the (static) capillary pressures for drainage and imbibition, whereas $p_{c,loc}$ at the maximal saturation is exactly the static capillary pressure for the dynamic models. The phase-pressure difference $\langle p_I \rangle_I - \langle p_{II} \rangle_{II}$ (bottom-right) shows the same qualitative behaviour.*

5.2.4. Effect of a hysteretic contact angle. Finally, we consider the effect of a hysteretic contact angle model and compare it to the static and dynamic ones. As in the constant-width case, we use the dynamic contact angle model (5.8) with $\theta_s = \pi/3$ and the hysteretic contact angle model (5.9) with $\theta_a = \pi/4$ and $\theta_r = 5\pi/12$. We consider a drainage and imbibition cycle by choosing the time-dependent inlet pressure $p_{in}(t) = 9 - 4t$, and stop the simulations when the interface position returns to the inlet. The other parameters are taken from Table 5.2.

As before, the total flux q decreases faster, when the interface passes through the constriction, see Figure 5.16 (top). Note that the higher capillary pressure when passing the constriction counteracts the drainage, while it increases the imbibition speed. This results in a more negative velocity. In case of the hysteretic contact angle model, the interface position γ_1 stops in the constriction, while the pressure lies in between the (static) capillary pressures for drainage and imbibition, so that the local capillary pressure $p_{c,loc}$ and the phase-pressure difference $\langle p_I \rangle_I - \langle p_{II} \rangle_{II}$ are multi-valued at the maximal saturation. In contrast, the dynamic model yields a direct switching between drainage and imbibition, when $p_{c,loc}$ is exactly the static capillary pressure (at the maximal saturation), see Figure 5.16 (bottom). Hence, hysteresis also leads to higher deviations from the static capillary pressure and thus a smaller maximal saturation.

6. Conclusion. We have formally derived the asymptotic solution for the flow of two immiscible fluids in a two-dimensional thin strip of varying width, where the fluid-fluid interface is treated as a free boundary. The obtained effective models form a system of differential algebraic equations for the interface position and the total

flux, and are applicable to a wide range of viscosity ratios M, of slip lengths λ, as well as contact angle models. The resulting effective relations are a Darcy-type equation for the local flow, and a capillary pressure - saturation relationship involving dynamic effects.

We have discussed the effects of a varying pore width, of the viscosity ratio, of the slip length as well as of having a dynamic and a hysteretic contact angle law through numerical experiments. In particular, the results for a varying pore width show that the geometry has a large influence on the effective quantities and their behaviour. While dynamic effects occur even for a static contact angle model, hysteresis in the capillary pressure is only present when a hysteretic contact model is used.

The presented models and effective relations can be generalized to asymmetric as well as tube-like three-dimensional domains with heterogeneities in the contact angle. Furthermore, rough walls of type $w^\varepsilon(x_1) = w(x_1) + \varepsilon w^1(x_1/\varepsilon) + \mathcal{O}(\varepsilon)$ would strongly affect the shape and position of the interface. This needs to be investigated in the future. Our future work will focus on the radial-symmetric case in three dimensions including the effect of outer forces such as gravity. Such three-dimensional models can be further used in pore-network models or for upscaling in a bundle-of-tubes model.

REFERENCES

[1] G. ALLAIRE, *Homogenization of the stokes flow in a connected porous medium*, Asymptotic Anal., 2 (1989), pp. 203–222, https://doi.org/10.3233/ASY-1989-2302.

[2] G. ALLAIRE, *Homogenization of the navier-stokes equations with a slip boundary condition*, Communications on pure and applied mathematics, 44 (1991), pp. 605–641, https://doi.org/10.1002/cpa.3160440602.

[3] J. AURIAULT, *Nonsaturated deformable porous media: Quasistatics*, Transport in Porous Media, 2 (1987), pp. 45–64, https://doi.org/10.1007/BF00208536.

[4] T. A. BAER, R. A. CAIRNCROSS, R. SCHUNK, R. R. RAO, AND P. A. SACKINGER, *A finite element method for free surface flows of incompressible fluids in three dimensions. Part II. Dynamic wetting lines*, Int. J. Numer. Meth. Fluids, 33 (2000), pp. 405–427, https://doi.org/10.1002/1097-0363(20000615)33:3<405::AID-FLD14>3.0.CO;2-4.

[5] A. BASSON AND D. GÉRARD-VARET, *Wall laws for fluid flows at a boundary with random roughness*, Communications on Pure and Applied Mathematics, 61 (2008), pp. 941–987, https://doi.org/10.1002/cpa.20237.

[6] A. Y. BELIAEV AND S. M. HASSANIZADEH, *A theoretical model of hysteresis and dynamic effects in the capillary relation for two-phase flow in porous media*, Transp. Porous Med., 43 (2001), pp. 487–510.

[7] A. Y. BELIAEV AND R. J. SCHOTTING, *Analysis of a new model for unsaturated flow in porous media including hysteresis and dynamic effects*, Computational Geosciences, 5 (2001), pp. 345–368.

[8] A. BELJADID, L. CUETO-FELGUEROSO, AND R. JUANES, *A continuum model of unstable infiltration in porous media endowed with an entropy function*, Advances in Water Resources, 144 (2020), p. 103684, https://doi.org/10.1016/j.advwatres.2020.103684.

[9] T. D. BLAKE, *Dynamic contact angles and wetting kinetics*, in Wettability, J. C. Berg, ed., Marcel Dekker, New York, 1993, pp. 251–309.

[10] T. D. BLAKE, *The physics of moving wetting lines*, Journal of Colloid and Interface Science, 299 (2006), pp. 1–13, https://doi.org/10.1016/j.jcis.2006.03.051.

[11] T. D. Blake and J. M. Haynes, *Kinetics of liquid/liquid displacement*, J. Colloid Interface Sci., 30 (1969), pp. 421–423, https://doi.org/10.1016/0021-9797(69)90411-1.

[12] D. Bonn, J. Eggers, J. Indekeu, J. Meunier, and E. Rolley, *Wetting and spreading*, Rev. Mod. Phys., 81 (2009), pp. 739–805, https://doi.org/10.1103/RevModPhys.81.739.

[13] S. Bottero, S. M. Hassanizadeh, P. J. Kleingeld, and T. J. Heimovaara, *Nonequilibrium capillarity effects in two-phase flow through porous media at different scales*, Water Resour. Res., 47 (2011), p. W10505.

[14] C. Bringedal, I. Berre, I. S. Pop, and F. A. Radu, *A model for non-isothermal flow and mineral precipitation and dissolution in a thin strip*, Journal of Computational and Applied Mathematics, 289 (2015), pp. 346–355, https://doi.org/10.1016/j.cam.2014.12.009.

[15] B. W. Cherry and C. M. Holmes, *Kinetics of wetting of surfaces by polymers*, J. Colloid Interface Sci., 29 (1969), pp. 174–176, https://doi.org/10.1016/0021-9797(69)90367-1.

[16] R. G. Cox, *The dynamics of the spreading of liquids on a solid surface. Part 1. Viscous flow*, J. Fluid Mech., 168 (1986), pp. 169–194, https://doi.org/10.1017/S0022112086000332.

[17] J. H. Cushman, L. S. Bennethum, and B. X. Hu, *A primer on upscaling tools for porous media*, Advances in Water Resources, 25 (2002), pp. 1043–1067, https://doi.org/10.1016/S0309-1708(02)00047-7.

[18] H. P. G. Darcy, *Les Fontaines publiques de la ville de Dijon. Exposition et application des principes à suivre et des formules à employer dans les questions de distribution d'eau, etc*, V. Dalamont, 1856.

[19] P. G. de Gennes, *Wetting: Statics and dynamics*, Rev. Mod. Phys., 57 (1985), pp. 827–863, https://doi.org/10.1103/RevModPhys.57.827.

[20] D. A. DiCarlo, *Experimental measurements of saturation overshoot on infiltration*, Water Resour. Res., 40 (2004), p. W04215.

[21] F. Doster, P. A. Zegeling, and R. Hilfer, *Numerical solutions of a generalized theory for macroscopic capillarity*, Physical Review E, 81 (2010), p. 036307.

[22] E. B. Dussan V., *On the spreading of liquids on solid surfaces: Static and dynamic contact lines*, Annu. Rev. Fluid Mech., 11 (1979), pp. 371–400, https://doi.org/10.1146/annurev.fl.11.010179.002103.

[23] E. B. Dussan V. and S. H. Davis, *On the motion of a fluid-fluid interface along a solid surface*, Journal of Fluid Mechanics, 65 (1974), pp. 71–95, https://doi.org/10.1017/S0022112074001261.

[24] R. J. Glass, T. S. Steenhuis, and J.-Y. Parlange, *Mechanism for finger persistence in homogeneous, unsaturated, porous media: Theory and verification*, Soil Science, 148 (1989), pp. 60–70.

[25] H. P. Greenspan, *On the motion of a small viscous droplet that wets a surface*, Journal of Fluid Mechanics, 84 (1978), pp. 125–143, https://doi.org/10.1017/S0022112078000075.

[26] D. Gérard-Varet and N. Masmoudi, *Relevance of the slip condition for fluid flows near an irregular boundary*, Communications in Mathematical Physics, 295 (2010), pp. 99–137, https://doi.org/10.1007/s00220-009-0976-0.

[27] P. J. Haley and M. J. Miksis, *The effect of the contact line on droplet spreading*, Journal of Fluid Mechanics, 223 (1991), pp. 57–81, https://doi.org/10.1017/S0022112091001337.

[28] S. M. Hassanizadeh and W. G. Gray, *General conservation equations for multi-phase systems: 1. Averaging procedure*, Advances in Water Resources, 2 (1979), pp. 131–144.

[29] S. M. Hassanizadeh and W. G. Gray, *Thermodynamic basis of capillary pressure in porous media*, Water Resources Research, 29 (1993), pp. 3389–3405, https://doi.org/10.1029/93WR01495.

[30] S. M. Hassanizadeh and W. G. Gray, *Toward an improved description of the physics of two-phase flow*, Advances in Water Resources, 16 (1993), pp. 53–67.

[31] R. Hilfer, *Capillary pressure, hysteresis and residual saturation in porous media*, Physica A: Statistical Mechanics and its Applications, 359 (2006), pp. 119–128, https://doi.org/10.1016/j.physa.2005.05.086.

[32] R. Hilfer, *Macroscopic capillarity and hysteresis for flow in porous media*, Physical Review E, 73 (2006), p. 016307.

[33] R. Hilfer, *Macroscopic capillarity without a constitutive capillary pressure function*, Physica A: Statistical Mechanics and its Applications, 371 (2006), pp. 209–225, https://doi.org/10.1016/j.physa.2006.04.051.

[34] R. Hilfer, F. Doster, and P. A. Zegeling, *Nonmonotone saturation profiles for hydrostatic equilibrium in homogeneous porous media*, Vadose Zone Journal, 11 (2012), pp. vzj2012–0021, https://doi.org/10.2136/vzj2012.0021.

[35] L. M. Hocking, *A moving fluid interface on a rough surface*, Journal of Fluid Mechanics, 76 (1976), pp. 801–817.

[36] U. Hornung, *Homogenization and Porous Media*, Springer, 1997.

[37] C. Huh and S. G. Mason, *Effects of surface roughness on wetting (theoretical)*, Journal of Colloid and Interface Science, 60 (1977), pp. 11–38, https://doi.org/10.1016/0021-9797(77)90251-X.

[38] C. Huh and S. G. Mason, *The steady movement of a liquid meniscus in a capillary tube*, Journal of Fluid Mechanics, 81 (1977), p. 401–419, https://doi.org/10.1017/S0022112077002134.

[39] C. Huh and L. E. Scriven, *Hydrodynamic model of steady movement of a solid/liquid/fluid contact line*, J. Colloid Interface Sci., 35 (1971), pp. 85–101.

[40] W. Jäger and A. Mikelić, *On the roughness-induced effective boundary conditions for an incompressible viscous flow*, Journal of Differential Equations, 170 (2001), pp. 96–122, https://doi.org/10.1006/jdeq.2000.3814.

[41] J. Koch, A. Rätz, and B. Schweizer, *Two-phase flow equations with a dynamic capillary pressure*, European Journal of Applied Mathematics, 24 (2013), pp. 49–75, https://doi.org/10.1017/S0956792512000307.

[42] J. Koplik and J. R. Banavar, *Continuum deductions from molecular hydrodynamics*, Annual Review of Fluid Mechanics, 27 (1995), pp. 257–292, https://doi.org/10.1146/annurev.fl.27.010195.001353.

[43] J. Koplik, J. R. Banavar, and J. F. Willemsen, *Molecular dynamics of Poiseuille flow and moving contact lines*, Phys. Rev. Lett., 60 (1988), pp. 1282–1285, https://doi.org/10.1103/PhysRevLett.60.1282.

[44] J. Koplik, J. R. Banavar, and J. F. Willemsen, *Molecular dynamics of fluid flow at solid surfaces*, Physics of Fluids A: Fluid Dynamics, 1 (1989), pp. 781–794, https://doi.org/10.1063/1.857376.

[45] K. Kumar, T. L. van Noorden, and I. S. Pop, *Effective dispersion equations for reactive flows involving free boundaries at the microscale*, Multiscale Modeling & Simulation, 9 (2011), pp. 29–58, https://doi.org/10.1137/100804553.

[46] A. Lamacz, A. Rätz, and B. Schweizer, *A well-posed hysteresis model for flows in porous media and applications to fingering effects*, Advances in Mathematical Sciences and Applications, 21 (2011), pp. 33–64.

[47] E. Marušić-Paloka, *Average of the Navier's law on the rapidly oscillating boundary*, Journal of Mathematical Analysis and Applications, 259 (2001), pp. 685–701, https://doi.org/10.1006/jmaa.2001.7505.

[48] A. Mikelić, *Homogenization of nonstationary navier-stokes equations in a domain with a grained boundary*, Annali di Matematica pura ed applicata, 158 (1991), pp. 167–179.

[49] A. Mikelić, *On an averaged model for the 2-fluid immiscible flow with surface tension in a thin cylindrical tube*, Computational Geosciences, 7 (2003), pp. 183–196, https://doi.org/10.1023/A:1025527716078.

[50] A. Mikelić and L. Paoli, *On the derivation of the Buckley-Leverett model from the two fluid Navier—Stokes equations in a thin domain*, Computational Geosciences, 1 (1997), pp. 59–83, https://doi.org/10.1023/A:1011509010432.

[51] K. Mitra and C. J. van Duijn, *Wetting fronts in unsaturated porous media: The combined case of hysteresis and dynamic capillary pressure*, Nonlinear Analysis: Real World Applications, 50 (2019), pp. 316–341, https://doi.org/10.1016/j.nonrwa.2019.05.005.

[52] N. R. Morrow and C. C. Harris, *Capillary equilibrium in porous materials*, Society of Petroleum Engineers Journal, 5 (1965), pp. 15–24, https://doi.org/10.2118/1011-PA.

[53] J. C. Parker and R. J. Lenhard, *A model for hysteretic constitutive relations governing multiphase flow: 1. saturation-pressure relations*, Water Resources Research, 23 (1987), pp. 2187–2196, https://doi.org/10.1029/WR023i012p02187.

[54] D. Picchi and I. Battiato, *The impact of pore-scale flow regimes on upscaling of immiscible two-phase flow in porous media*, Water Resources Research, 54 (2018), pp. 6683–6707, https://doi.org/10.1029/2018WR023172.

[55] M. Quintard and S. Whitaker, *Two-phase flow in heterogeneous porous media: The method of large-scale averaging*, Transport in Porous Media, 3 (1988), pp. 357–413, https://doi.org/10.1007/BF00233177.

[56] J. Ralston, M. Popescu, and R. Sedev, *Dynamics of wetting from an experimental point of view*, Annu. Rev. Mater. Res., 38 (2008), pp. 23–43, https://doi.org/10.1146/annurev.matsci.38.060407.130231.

[57] W. Ren and W. E, *Boundary conditions for the moving contact line problem*, Physics of Fluids, 19 (2007), p. 022101, https://doi.org/10.1063/1.2646754.

[58] W. Ren, D. Hu, and W. E, *Continuum models for the contact line problem*, Physics of Fluids, 22 (2010), p. 102103, https://doi.org/10.1063/1.3501317.

[59] L. A. RICHARDS, *Capillary conduction of liquids through porous mediums*, Physics, 1 (1931), pp. 318–333.

[60] A. RÄTZ AND B. SCHWEIZER, *Hysteresis models and gravity fingering in porous media*, ZAMM - Zeitschrift für Angewandte Mathematik und Mechanik, 94 (2014), pp. 645–654, https://doi.org/10.1002/zamm.201200052.

[61] B. SCHWEIZER, *Hysteresis in porous media: Modelling and analysis*, Interfaces Free Bound, 19 (2017), pp. 417–447.

[62] S. SHARMIN, C. BRINGEDAL, AND I. S. POP, *On upscaling pore-scale models for two-phase flow with evolving interfaces*, Advances in Water Resources, 142 (2020), p. 103646, https://doi.org/10.1016/j.advwatres.2020.103646.

[63] P. SHENG AND M. ZHOU, *Immiscible-fluid displacement: Contact-line dynamics and the velocity-dependent capillary pressure*, Phys. Rev. A, 45 (1992), pp. 5694–5708, https://doi.org/10.1103/PhysRevA.45.5694.

[64] S. SHIOZAWA AND H. FUJIMAKI, *Unexpected water content profiles under flux-limited one-dimensional downward infiltration in initially dry granular media*, Water Resources Research, 40 (2004), p. W07404, https://doi.org/10.1029/2003WR002197.

[65] Y. SUI, H. DING, AND P. D. SPELT, *Numerical simulations of flows with moving contact lines*, Annual Review of Fluid Mechanics, 46 (2014), pp. 97–119, https://doi.org/10.1146/annurev-fluid-010313-141338.

[66] THE MATHWORKS INC., *MATLAB® version 9.8.0.1417392 (R2020a)*, 2020, http://www.mathworks.com/products/matlab.html.

[67] P. A. THOMPSON, W. B. BRINCKERHOFF, AND M. O. ROBBINS, *Microscopic studies of static and dynamic contact angles*, Journal of Adhesion Science and Technology, 7 (1993), pp. 535–554, https://doi.org/10.1163/156856193X00844.

[68] P. A. THOMPSON AND M. O. ROBBINS, *Simulations of contact-line motion: Slip and the dynamic contact angle*, Phys. Rev. Lett., 63 (1989), pp. 766–769, https://doi.org/10.1103/PhysRevLett.63.766.

[69] C. J. VAN DUIJN, Y. FAN, L. A. PELETIER, AND I. S. POP, *Travelling wave solutions for degenerate pseudo-parabolic equations modelling two-phase flow in porous media*, Nonlinear Analysis: Real World Applications, 14 (2013), pp. 1361–1383, https://doi.org/10.1016/j.nonrwa.2012.10.002.

[70] C. J. VAN DUIJN AND K. MITRA, *Hysteresis and horizontal redistribution in porous media*, Transport in Porous Media, 122 (2018), pp. 375–399, https://doi.org/10.1007/s11242-018-1009-2.

[71] T. L. VAN NOORDEN, *Crystal precipitation and dissolution in a thin strip*, European Journal of Applied Mathematics, 20 (2009), pp. 69–91, https://doi.org/10.1017/S0956792508007651.

[72] O. V. VOINOV, *Hydrodynamics of wetting*, Fluid Dynamics, 11 (1976), pp. 714–721, https://doi.org/10.1007/BF01012963.

[73] S. WHITAKER, *Flow in porous media II: The governing equations for immiscible, two-phase flow*, Transport in Porous Media, 1 (1986), pp. 105–125.

[74] L. ZHUANG, S. M. HASSANIZADEH, C.-Z. QIN, AND A. DE WAAL, *Experimental investigation of hysteretic dynamic capillarity effect in unsaturated flow*, Water Resources Research, 53 (2017), pp. 9078–9088, https://doi.org/10.1002/2017WR020895.

[75] L. ZHUANG, S. M. HASSANIZADEH, C. VAN DUIJN, S. ZIMMERMANN, I. ZIZINA, AND R. HELMIG, *Experimental and numerical studies of saturation overshoot during infiltration into a dry soil*, Vadose Zone Journal, 18 (2019), https://doi.org/10.2136/vzj2018.09.0167.

UHasselt Computational Mathematics Preprint Series

2020

UP-20-06 *S.B. Lunowa, C. Bringedal, I.S. Pop*, **On an averaged model for immiscible two-phase flow with surface tension and dynamic contact angle in a thin strip**, 2020

UP-20-05 *M. Bastidas Olivares, C. Bringedal, I.S. Pop*, **An adaptive multiscale iterative scheme for a phase-field model for precipitation and dissolution in porous media**, 2020

UP-20-04 *C. Cancès, J. Droniou, C. Guichard, G. Manzini, M. Bastidas Olivares, I.S. Pop*, **Error estimates for the gradient discretisation of degenerate parabolic equation of porous medium type**, 2020

UP-20-03 *S.B. Lunowa, I.S. Pop, and B. Koren*, **Linearization and Domain Decomposition Methods for Two-Phase Flow in Porous Media Involving Dynamic Capillarity and Hysteresis**, 2020

UP-20-02 *M. Bastidas, C. Bringedal, and I.S. Pop*, **Numerical simulation of a phase-field model for reactive transport in porous media**, 2020

UP-20-01 *S. Sharmin, C. Bringedal, and I.S. Pop*, **Upscaled models for two-phase flow in porous media with evolving interfaces at the pore scale**, 2020

2019

UP-19-17 *C. Bringedal*, **A conservative phase-field model for reactive transport**, 2019

UP-19-16 *D. Landa-Marbán, G. Bødtker, B.F. Vik, P. Pettersson, I.S. Pop, K. Kumar, F.A. Radu*, **Mathematical Modeling, Laboratory Experiments, and Sensitivity Analysis of Bioplug Technology at Darcy Scale**, 2019

UP-19-15 *D. Illiano, I.S. Pop, F.A. Radu*, **An efficient numerical scheme for fully coupled flow and reactive transport in variably saturated porous media including dynamic capillary effects**, 2019

UP-19-14 *S.B. Lunowa, I.S. Pop, and B. Koren*, **A Linear Domain Decomposition Method for Non-Equilibrium Two-Phase Flow Models**, 2019

UP-19-13 *C. Engwer, I.S. Pop, T. Wick*, **Dynamic and weighted stabilizations of the L-scheme applied to a phase-field model for fracture propagation**, 2019

UP-19-12 *M. Gahn*, **Singular limit for quasi-linear diffusive transport through a thin heterogeneous layer**, 2019

UP-19-11 *M. Gahn, W. Jäger, M. Neuss-Radu*, **Correctors and error estimates for reaction-diffusion processes through thin heterogeneous layers in case of homogenized equations with interface diffusion**, 2019

UP-19-10 *V. Kučera, M. Lukáčová-Medvidová, S. Noelle, J. Schütz,*, **Asymptotic properties of a class of linearly implicit schemes for weakly compressible Euler equations**, 2019

UP-19-09 *D. Seal, J. Schütz*, **An asymptotic preserving semi-implicit multiderivative solver**, 2019

UP-19-08 *H. Hajibeygi, M. Bastidas Olivares, M. HosseiniMehr, I.S. Pop, M.F. Wheeler*, **A benchmark study of the multiscale and homogenization methods for fully implicit multiphase ow simulations with adaptive dynamic mesh (ADM)**, 2019

UP-19-07 *J.W. Both, I.S. Pop, I. Yotov*, **Global existence of a weak solution to unsaturated poroelasticity**, 2019

UP-19-06 *K. Mitra, T. Köppl, I.S. Pop, C.J. van Duijn, R. Helmig*, **Fronts in two-phase porous flow problems: effects of hysteresis and dynamic capillarity**, 2019

UP-19-05 *D. Illiano, I.S. Pop, F.A. Radu*, **Iterative schemes for surfactant transport in porous media**, 2019

UP-19-04 *M. Bastidas, C. Bringedal, I.S. Pop, F.A. Radu*, **Adaptive numerical homogenization of nonlinear diffusion problems**, 2019

UP-19-03 *K. Kumar, F. List, I.S. Pop, F.A. Radu*, **Formal upscaling and numerical validation of fractured flow models for Richards′ equation**, 2019

UP-19-02 *M.A. Endo Kokubun, A. Muntean, F.A. Radu, K. Kumar, I.S. Pop, E. Keilegavlen, K. Spildo*, **A pore-scale study of transport of inertial particles by water in porous media**, 2019

UP-19-01 *C. Bringedal, L. von Wolff, and I.S. Pop*, **Phase field modeling of precipitation and dissolution processes in porous media: Upscaling and numerical experiments**, 2019